Supplementary information

Safe electrolyte design with isolated solvation nanoclusters for high-energy lithium metal batteries

Jimin Tang[1], Zhuangzhuang Cui[2], Zhixuan Wei[1,*], Guowei Zeng[1], Chunyu Wang[3], Zizhun Wang[4], Wei Zhang[4], Heng Jiang[1,*], Fei Du[1,*]

[1]*Key Laboratory of Physics and Technology for Advanced Batteries (Ministry of Education), College of Physics, Jilin University, Changchun 130012, China*

[2] *Hefei National Research Center for Physical Sciences at the Microscale, School of Chemistry and Materials Science, University of Science and Technology of China, Hefei 230026, China.*

[3]*State Key Laboratory of Supramolecular Structure and Materials, College of Chemistry, Jilin University, Changchun 130012, China*

[4]*Electron Microscopy Center, Jilin University, Changchun 130012, China*

**Corresponding Author: zhixuanwei@jlu.edu.cn; jiangheng@jlu.edu.cn; dufei@jlu.edu.cn*

Supplementary Figures

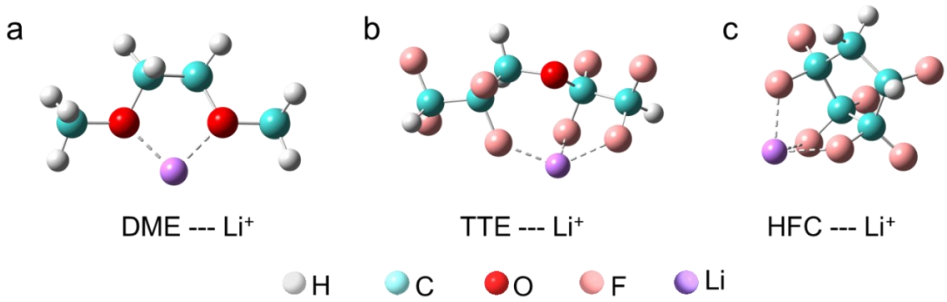

Supplementary Figure 1. Molecular structures and binding sites of Li^+ with (a) DME, (b) TTE, and (c) HFC molecules.

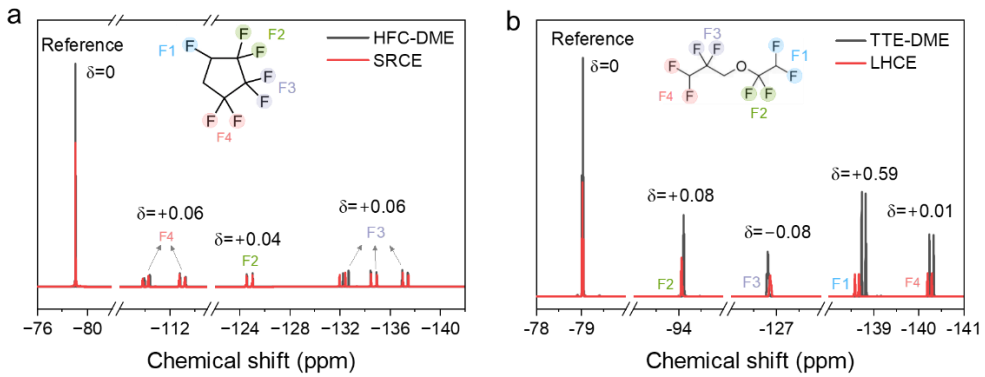

Supplementary Figure 2. Investigation of Li^+ and diluents coordination. The ^{19}F NMR spectrum of (a) DME/HFC mixture and SRCE and (b) DME/TTE mixture and LHCE. Note: Due to the multiplet structure of HFC caused by F-F spin-spin coupling, its chemical shift was calculated by averaging the highest peaks within each split signal[1].

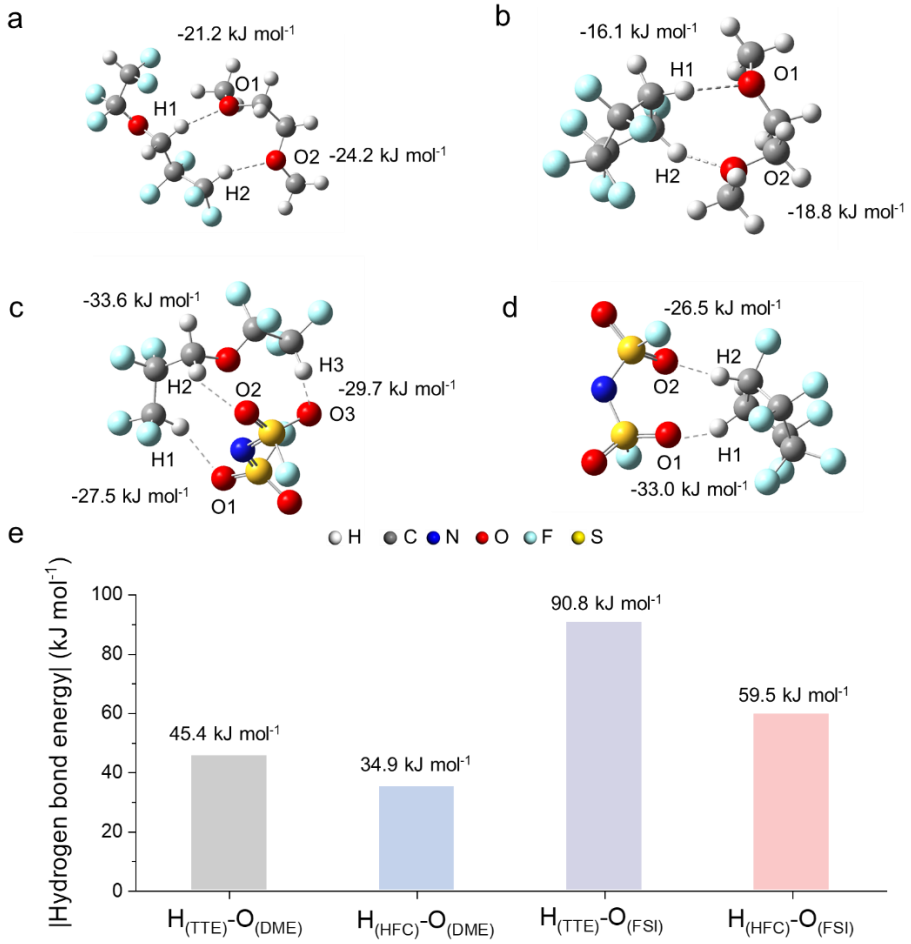

Supplementary Figure 3. Comparative analysis of hydrogen-bonding interactions between diluents and electrolyte components. (a-b) Optimized binding configurations and the calculated individual hydrogen-bond energies between the DME solvent and the (a) TTE and (b) HFC diluent molecules. (c-d) Optimized binding configurations and the calculated individual hydrogen-bond energies between the FSI^- anion and the (c) TTE and (d) HFC diluent molecules. (e) Comparison of the total absolute hydrogen-bond binding energies for the respective diluent-solvent and diluent-anion interactions.

Supplementary Note 1.

DFT calculations based on the Atoms in Molecules (AIM) theory were conducted to comparatively analyze the intermolecular interactions between the diluents (TTE and HFC) and the key electrolyte components, including the DME solvent and the FSI^- anion.

Firstly, for the diluent-solvent interactions, the hydrogen bonds (H-bonds) involving $CH_3O\cdots H$ interactions show stronger bonding energies of -21.6 and -24.2 kJ mol^{-1}, higher than those (-16.1

and -18.8 kJ mol^{-1}) in the HFC-DME system (**Supplementary Figure 3 a, b**). The total absolute H-bond energy between HFC and DME (34.9 kJ mol^{-1}) is lower than that of the TTE-DME system (45.4 kJ mol^{-1}), indicating that HFC has a weaker tendency to anchor or perturb the solvent molecules (**Supplementary Figure 3e**). More importantly, the interactions between the diluents and the FSI^- anion were further scrutinized. The TTE molecule coordinates with the FSI^- anion via three distinct H-bonds (-33.6, -27.5, and -29.7 kJ mol^{-1}), resulting in a high total binding energy of 90.8 kJ mol^{-1}. In contrast, the HFC-FSI^- interaction is weaker, characterized by only two H-bonds (-33.0 and -26.5 kJ mol^{-1}) with a much lower total energy of 59.5 kJ mol^{-1} (**Supplementary Figure 3 c-e**). These quantitative results provide model-dependent support that the HFC diluent exhibits weak interactions with both solvents and anions due to its cyclic structure and lower polarizability. This phenomenon of HFC is consistent with weaker perturbation of the primary anion-rich solvation shell, promoting the formation of smaller, isolated solvation nanoclusters as discussed in the main text.

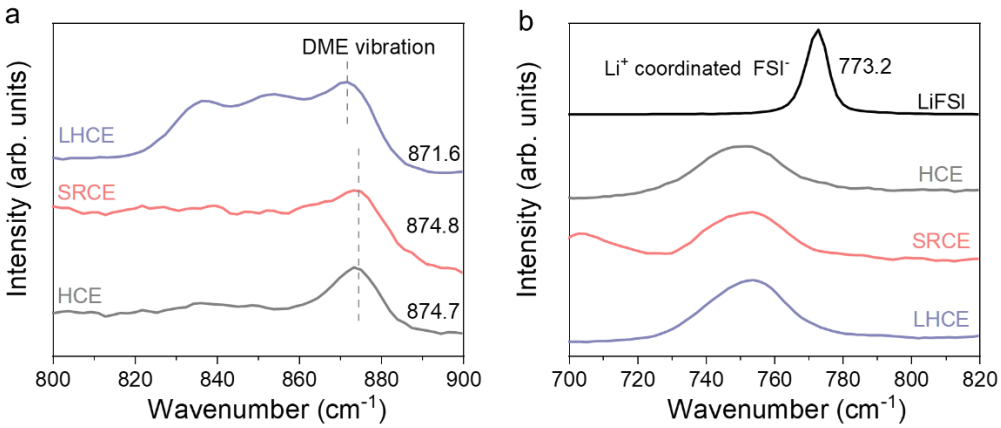

Supplementary Figure 4. Probing Li^+ solvation structure via Raman spectroscopy. (a) Raman shifts for the characteristic vibration modes of DME. (b) Raman shifts for the S-N-S bending mode of the FSI^-.

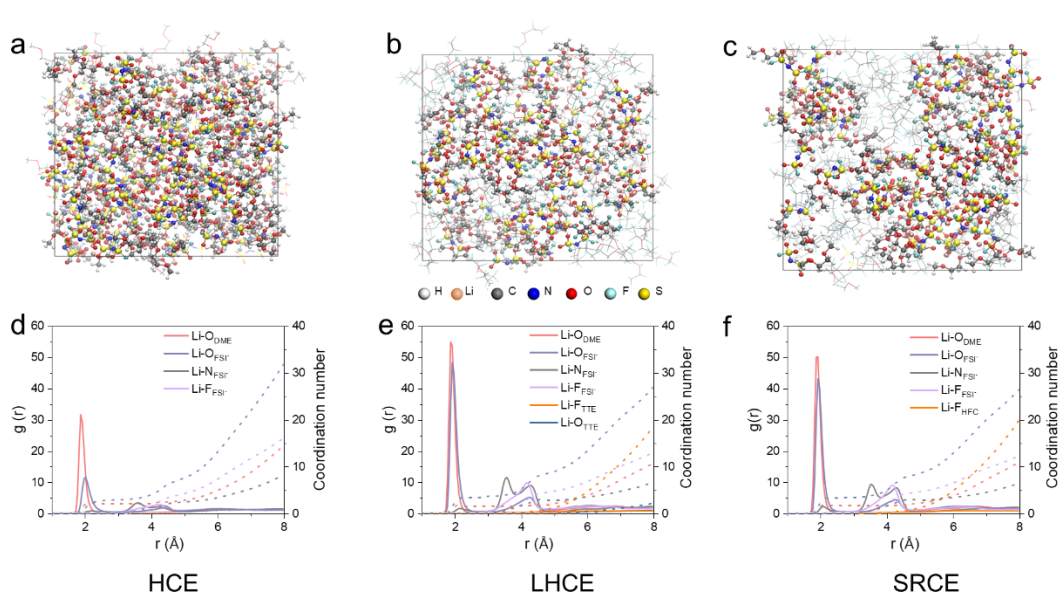

Supplementary Figure 5. Molecular dynamics (MD) simulations reveal distinct solvation structures. Representative MD snapshots and the corresponding radial distribution functions (RDFs) and coordination numbers (CNs) profiles for (a, d) HCE, (b, e) LHCE, and (c, f) SRCE.

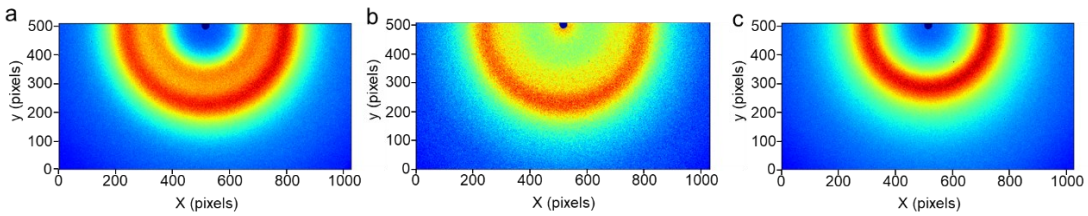

Supplementary Figure 6. Synchrotron-wide-angle X-ray scattering (WAXS) patterns. Snapshots obtained for (a) HCE, (b) LHCE, and (c) SRCE electrolytes.

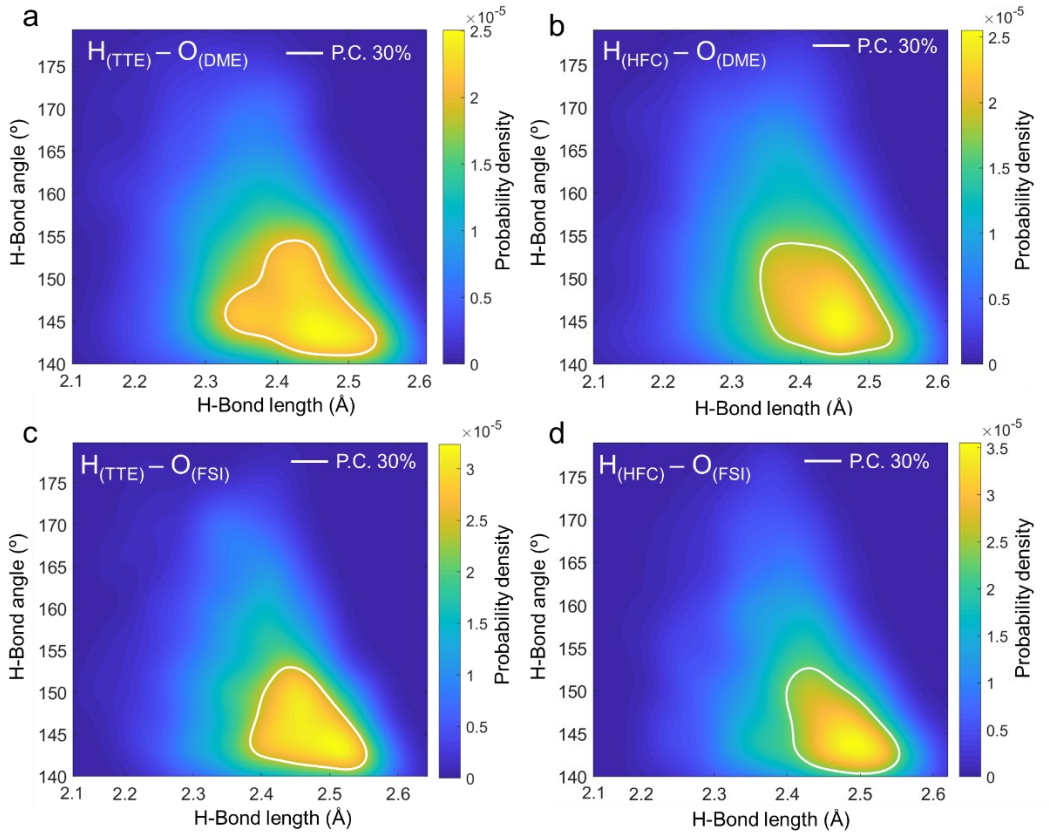

Supplementary Figure 7. Hydrogen-bonding interactions between diluents and electrolyte components. Distributions of hydrogen bond lengths and angles: (a) between TTE (H) and DME (O) in LHCE, (b) between HFC (H) and DME (O) in SRCE, (c) between TTE (H) and FSI^- (O) in LHCE, and (d) between HFC (H) and FSI^- (O) in SRCE. Note: probability contour (P.C.).

Supplementary Note 2.

A comparative analysis of H-bond lengths and angles was also performed to understand the interactions between the diluents and the DME solvent or FSI^- (representing contact ion pairs). For clarity, the values of the 30% probability contour (P.C.) are used as reference benchmarks[2]. Aligning with the results in **Supplementary Figure 3**, the H-bonds between CH_3O- of DME and H in TTE have a tendency to shorten the bond length and shift the bond angle to be higher, indicating a stronger binding affinity than those between HFC and DME (**Supplementary Figure 7a-b**). Moreover, the interactions between diluents and FSI^- show a similar trend, contributing to the weaker hydrogen polarity and enhanced steric hindrance of the cyclic fluorinated alkane. Therefore, HFC molecules exhibit a larger HSP distance than CIPs, thereby promoting the isolation of CIPs into nanoclusters.

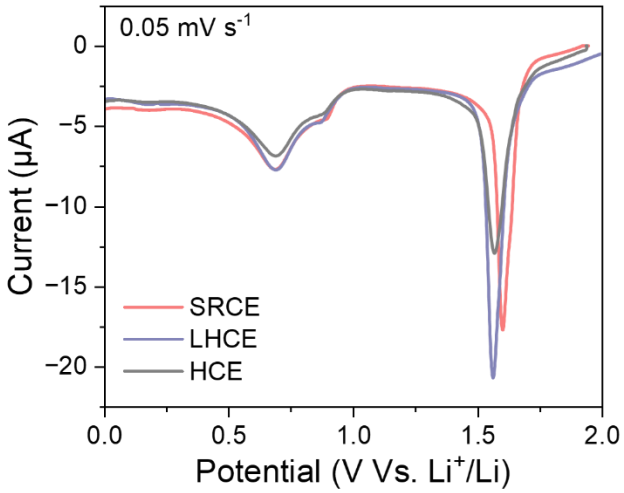

Supplementary Figure 8. Anion reduction stability probed by LSV. Current-potential profiles for Li||Cu cells scanned from open-circuit voltage to 0 V (vs. Li^+/Li) at 0.05 mV s^{-1} and at 25°C for three electrolytes[3].

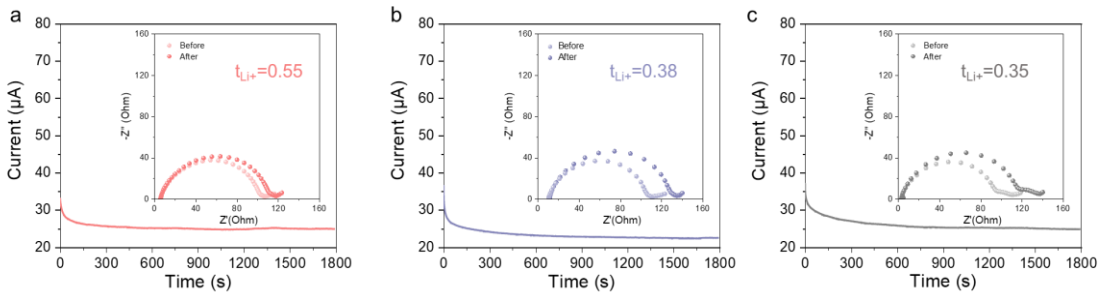

Supplementary Figure 9. Li^+ transference numbers (t_{Li^+}) measurements. Chronoamperometry (CA) curves of Li||Li symmetric cells at 25 °C with a constant polarization potential of 10 mV for (a)SRCE, (b) LHCE, and (c) HCE electrolytes. Inset: Corresponding Nyquist plots of the Li||Li symmetric cells before and after CA polarization.

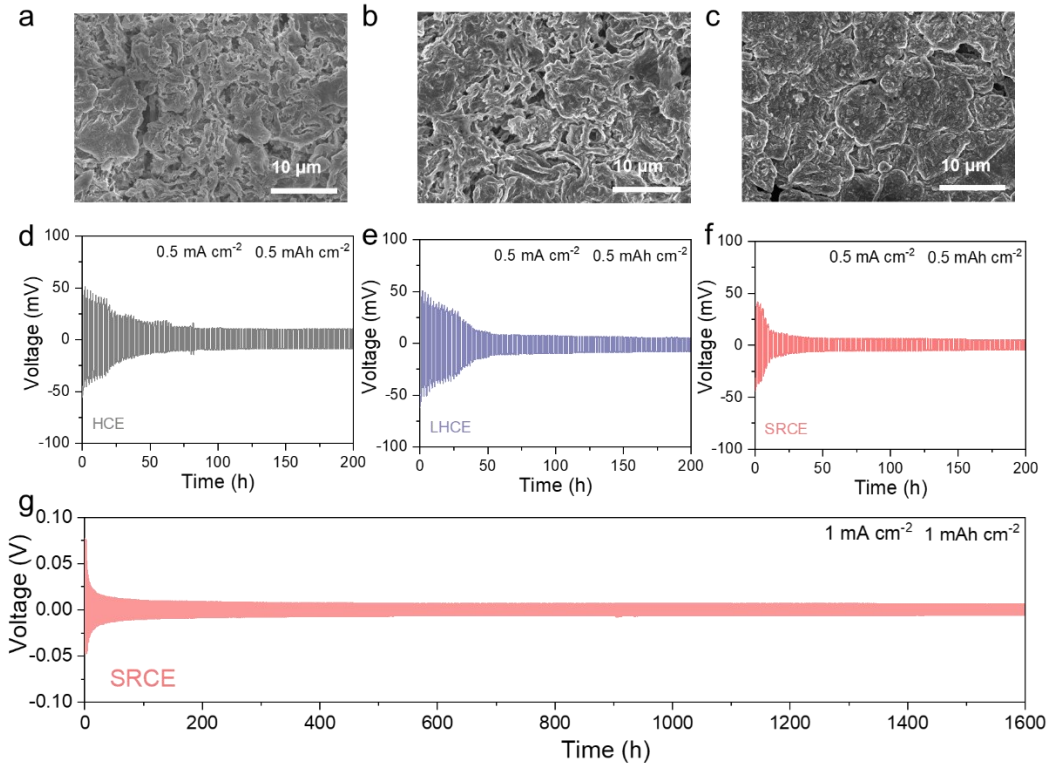

Supplementary Figure 10. Morphology of Li metal negative electrodes after Li plating/stripping and corresponding plating/stripping stability. (a-c) SEM images of Li metal negative electrode after 100 plating/stripping cycles in Li||Li symmetric cells at 25°C with 0.5 mA $cm^{-2}$and 0.5 mAh cm^{-2} for HCE (a), LHCE (b), and SRCE (c). (d-f) Corresponding voltage profiles of the same cells. (g) Long-term plating/stripping voltage profile of Li||Li symmetric cell at 25°C in SRCE at a current density of 1 mA cm^{-2} and areal capacity of 1 mAh cm^{-2}.

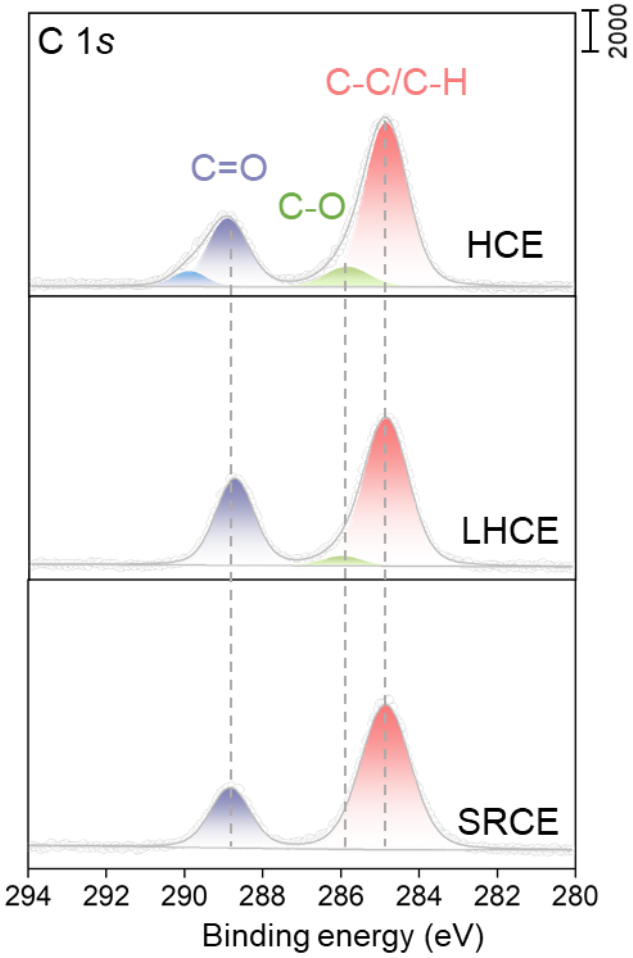

Supplementary Figure 11. XPS analysis of SEI composition. C 1*s* XPS spectra of SEI layers formed on Cu substrates after plating 5 mAh cm^{-2} of Li at 0.5 mA cm^{-2} and 25 °C in the three electrolytes.

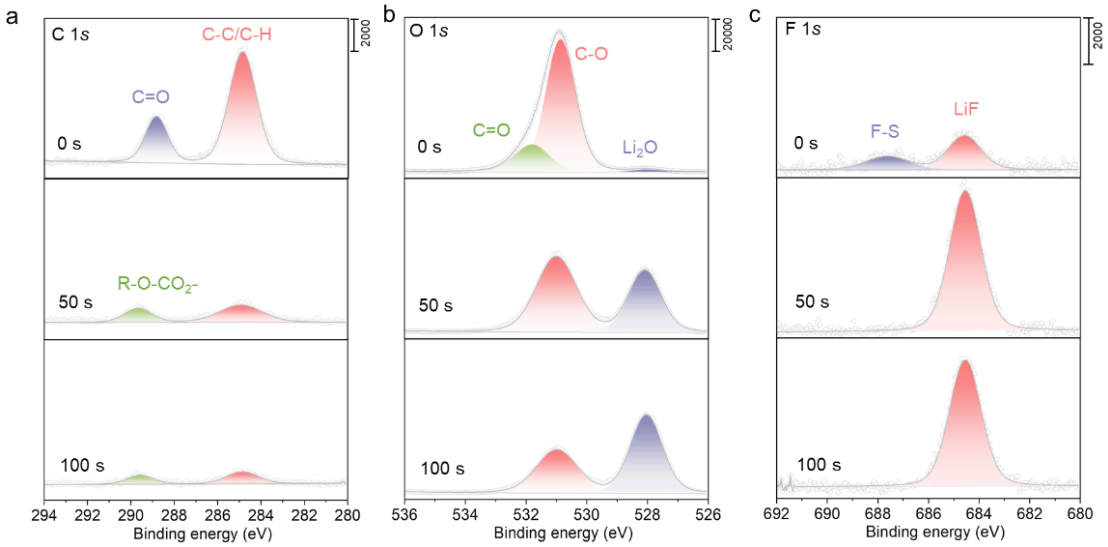

Supplementary Figure 12. XPS analysis of SEI composition. XPS results with depth profiles of (a) C 1*s*, (b) O 1*s*, and (c) F 1*s* spectra of at different sputtering times for the SEI formed in a Li||Cu cell with SRCE electrolyte after plating 3 mAh cm^{-2} of Li at 0.5 mA cm^{-2} and 25 °C.

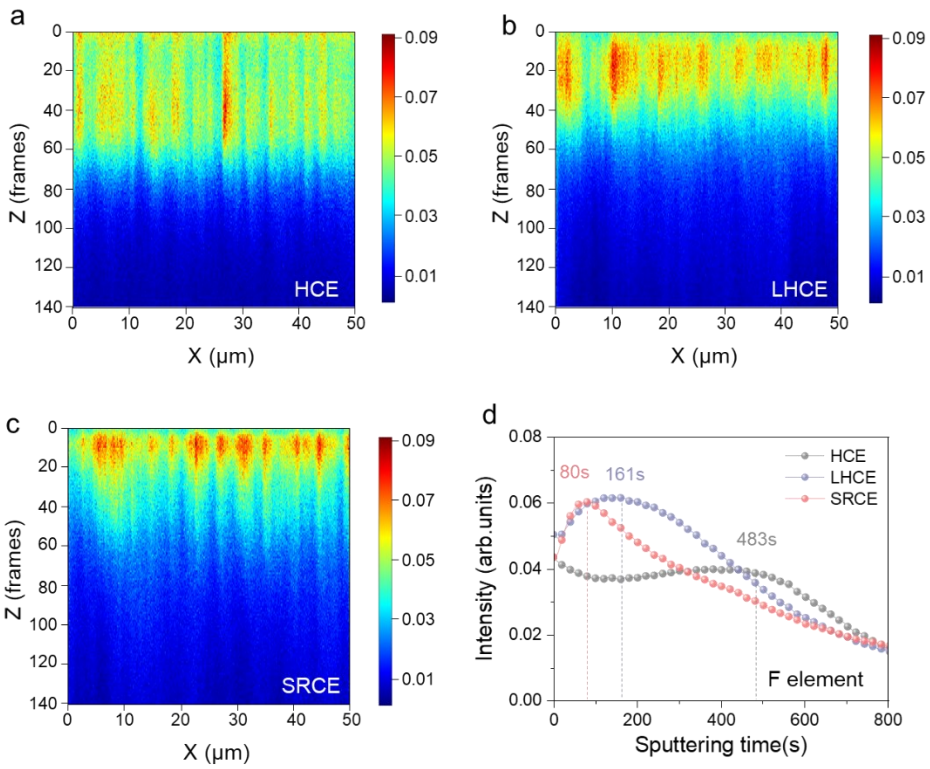

Supplementary Figure 13. Depth profiling of F^- distribution in the SEI by TOF-SIMS. (a-c) Two-dimensional TOF-SIMS maps showing the variation of F^- signal intensity as a function of sputtering depth for the SEI formed on Li metal electrodes after plating 5 mAh cm^{-2} of Li at 0.5 mA cm^{-2} and 25 °C in Li||Cu cells with (a) HCE, (b) LHCE, and (c) SRCE. (d) Corresponding F^- depth profiles under the same conditions.

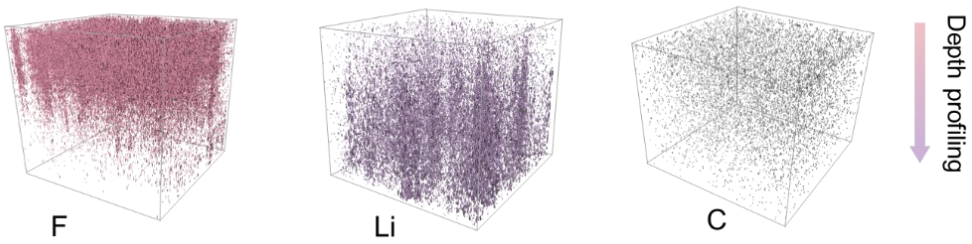

Supplementary Figure 14. 3D variation of the TOF-SIMS intensity related to the corresponding element fragments of LHCE-derived SEI. The 3D distribution of corresponding element fragments for the SEI formed after plating 5 mAh cm^{-2} of Li at 0.5 mA cm^{-2} and 25 °C in a Li||Cu cell with LHCE electrolyte.

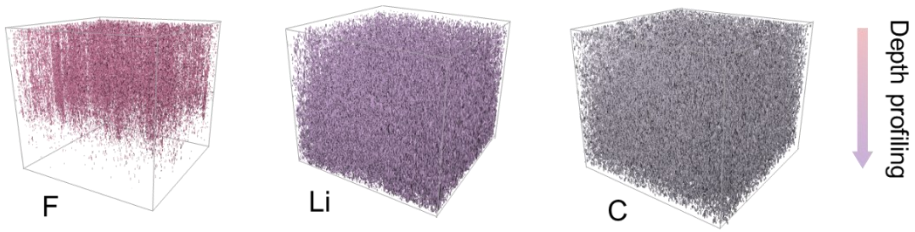

Supplementary Figure 15. 3D variation of the TOF-SIMS intensity related to the corresponding element fragments of HCE-derived SEI. The 3D distribution of corresponding element fragments for the SEI formed after plating 5 mAh cm^{-2} of Li at 0.5 mA cm^{-2} and 25 °C in a Li||Cu cell with HCE electrolyte.

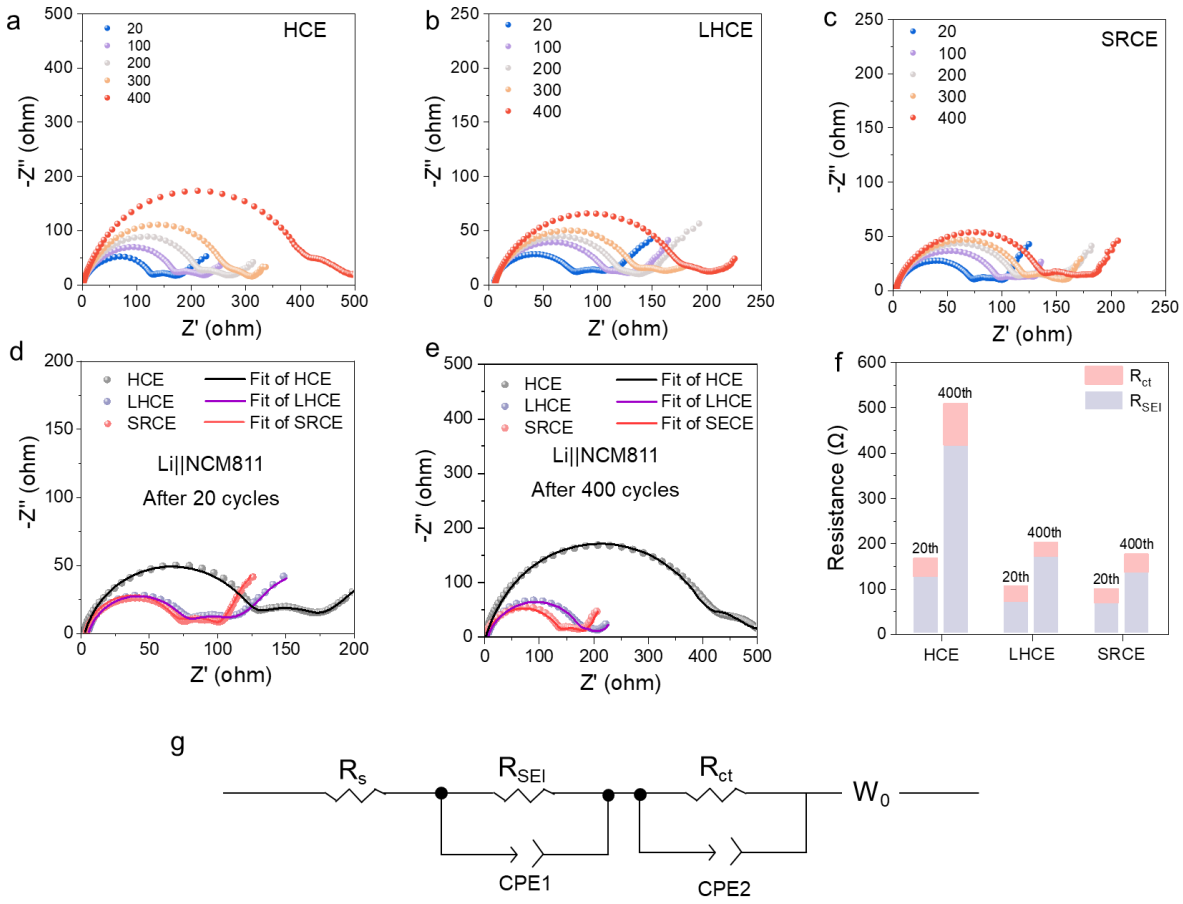

Supplementary Figure 16. Electrochemical impedance analysis of Li||NCM811 cells during cycling. Nyquist plots of cells with (a) HCE, (b) LHCE and (c) SRCE electrolytes, measured at different cycle numbers and at a temperature of 25 °C. (d-e) Experimental and fitted EIS spectra of the cells with the three electrolytes at the 20th and 400th cycles, respectively. The symbols represent the experimental impedance data, and the solid lines represent the corresponding equivalent-circuit fits. (f) A comparison of the fitted R_{SEI} and R_{ct} values at the 20th and 400th cycles. (g) Equivalent circuit model used to fit the EIS spectra. R_s, R_{SEI} and R_{ct} represent the ohmic, interphase and charge-transfer resistances respectively; CPE1 and CPE2 represent the corresponding non-ideal capacitances; and W_0 represents the Warburg diffusion element.

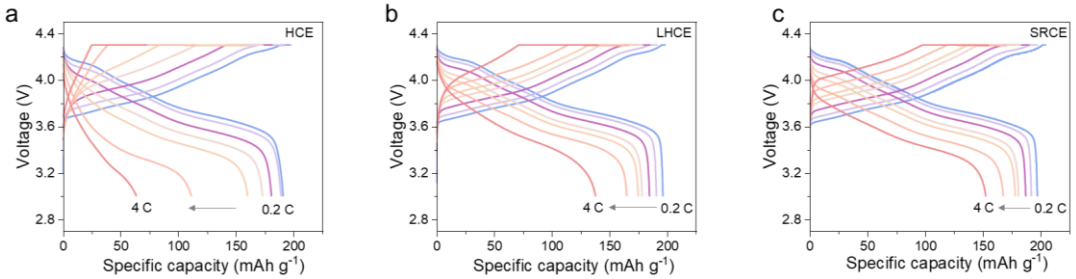

Supplementary Figure 17. Rate capability evaluation of 50 µm Li||2.5 mAh cm^{-2} NCM811 coin cells with different electrolytes. Galvanostatic charge-discharge voltage profiles at 25°C in the voltage range of 3-4.3 V at progressively increasing current rates from 0.2 C, 0.5 C, 1 C, 1.5 C, 2 C, 3 C to 4 C for (a) HCE, (b) LHCE, and (c) SRCE. 1 C= 200 mA g^{-1}.

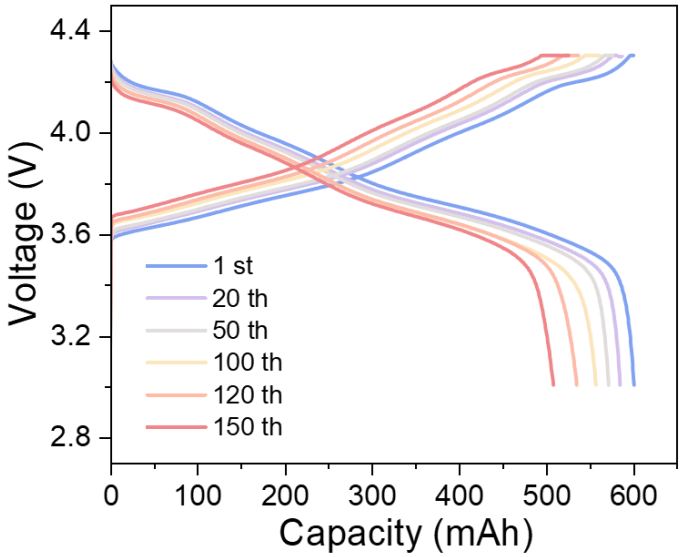

Supplementary Figure 18. Galvanostatic charge-discharge voltage profiles of a 600 mAh Li||NCM811 metal pouch cell at 25°C at selected cycle numbers.

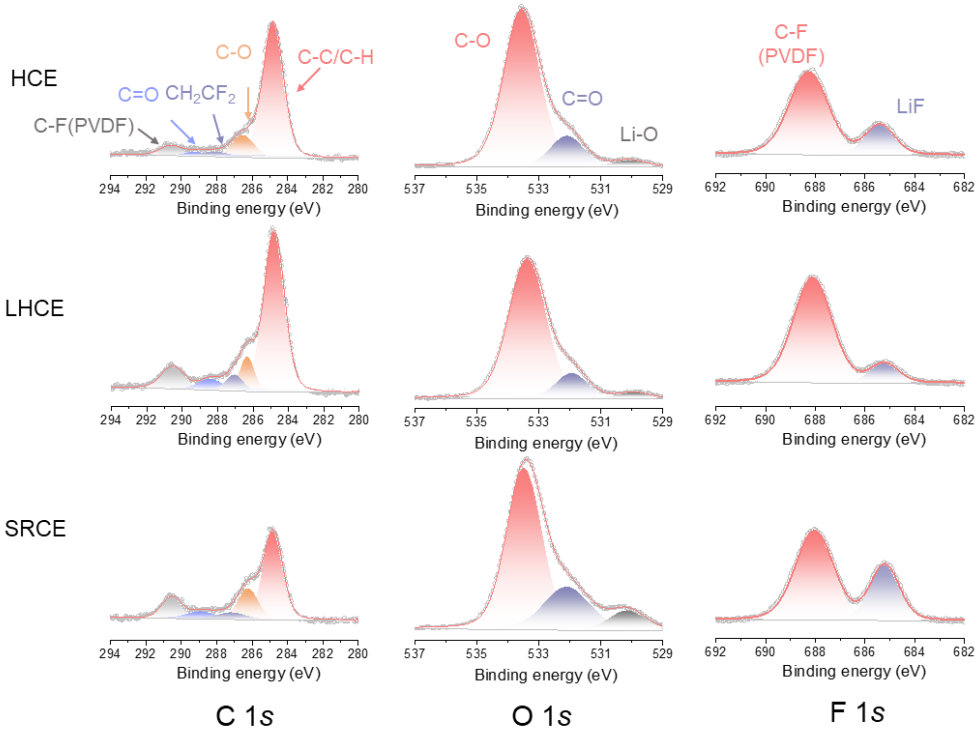

Supplementary Figure 19. CEI composition on NCM811 positive electrodes after 50 cycles in three electrolytes. XPS spectra of C 1*s*, O 1*s*, and F 1*s* for NCM811 positive electrodes after 50 cycles at 25°C in Li||2.5 mAh cm^{-2} NCM811 cells (0.5C charge/1C discharge, 3-4.3 V) with HCE, LHCE, and SRCE, respectively.

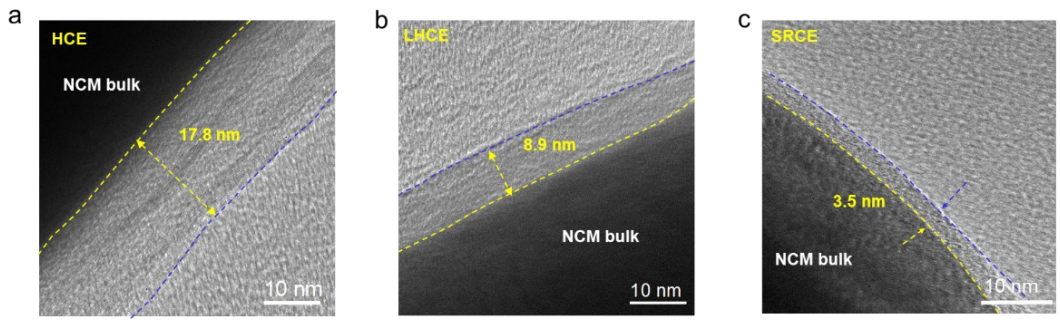

Supplementary Figure 20. Thickness of the CEI on NCM811 positive electrodes. High-resolution TEM images of the CEI layer formed on NCM811 positive electrodes after 50 cycles at 25°C in Li||2.5 mAh cm^{-2} NCM811 cells (0.5C charge/1C discharge, 3-4.3 V) in (a) HCE, (b) LHCE, and (c) SRCE.

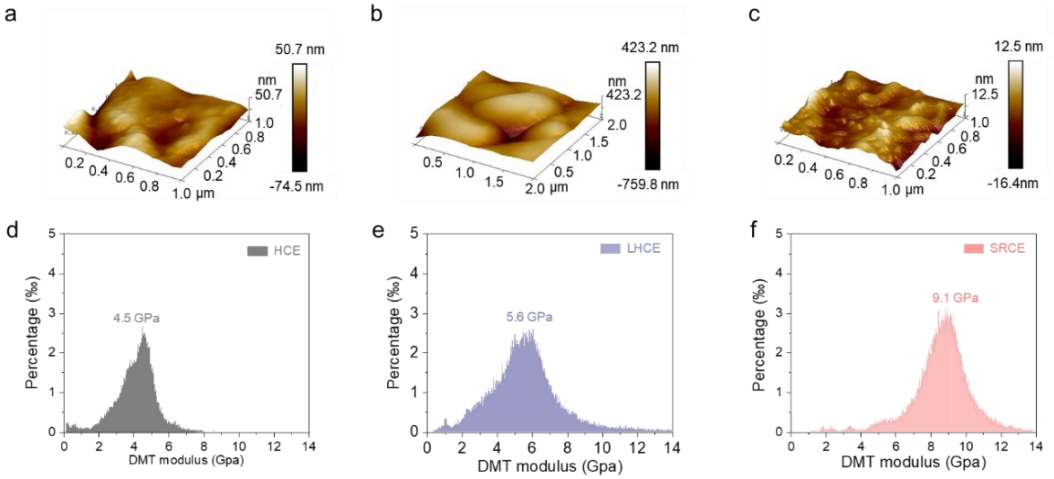

Supplementary Figure 21. Nanomechanical properties of the CEI on cycled NCM811 positive electrodes. (a-c) Topography and (d-f) corresponding Derjaguin-Muller-Toporov (DMT) modulus maps acquired by atomic force microscopy in quantitative nanomechanical mapping (AFM-QNM) mode for NCM811 positive electrodes after 50 cycles at 25 °C in Li||2.5 mAh cm^{-2} NCM811 cells (0.5C charge/1C discharge, 3-4.3 V) in (a, d) HCE, (b, e) LHCE, and (c, f) SRCE.

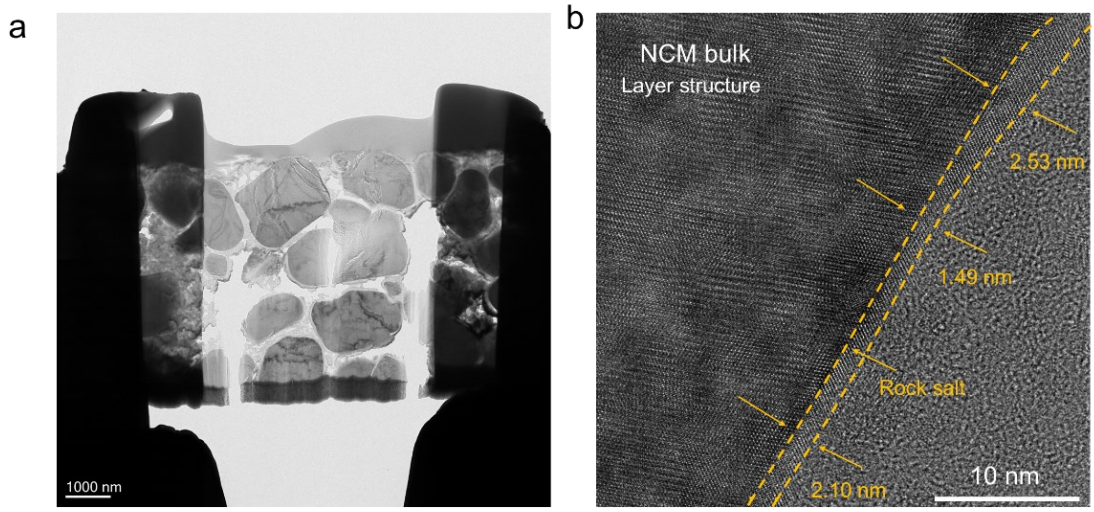

Supplementary Figure 22. Phase evolution on the cycled NCM811 positive electrode surface. STEM analysis of an NCM811 positive electrode particle after 200 cycles at 25 °C in a Li||2.5 mAh cm^{-2} NCM811 cells (0.5C charge/1C discharge, 3-4.3 V) with SRCE electrolyte. (a) TEM image of the FIB-prepared NCM811 particle. (b) High-resolution STEM image showing the layered structure in the bulk and a ~2 nm rock-salt layer at the surface.

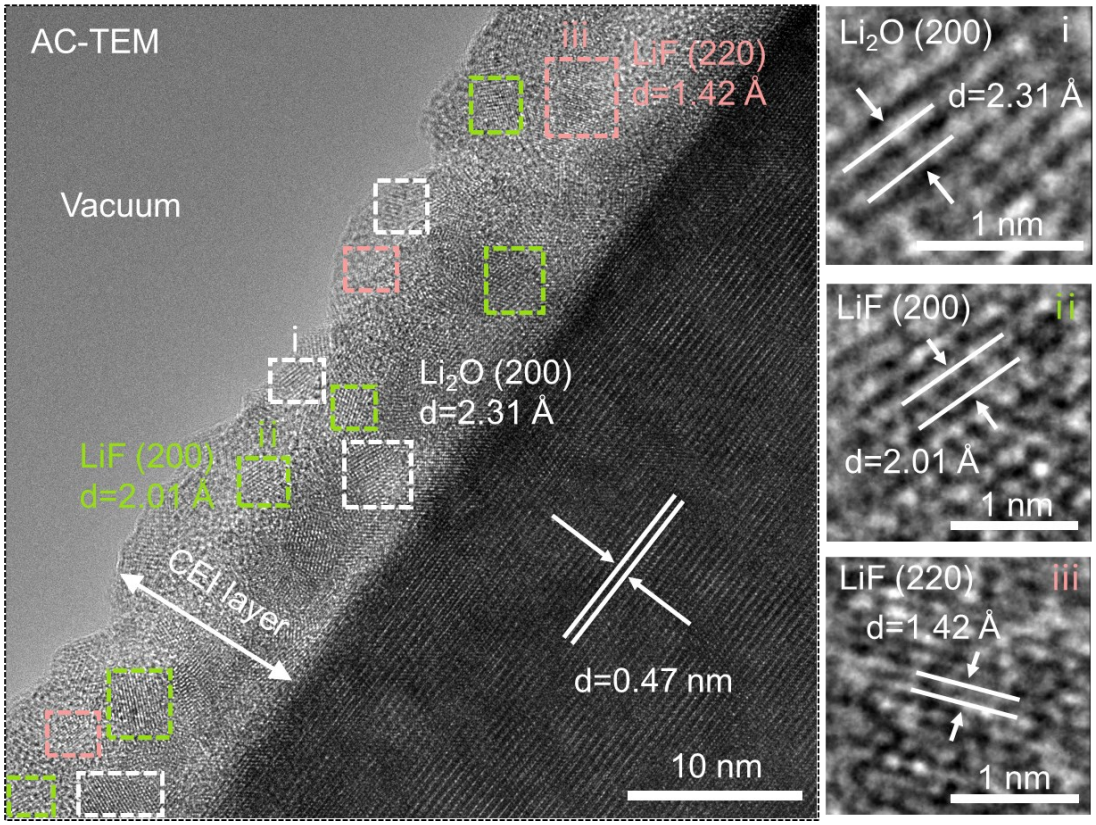

Supplementary Figure 23. Aberration-corrected TEM (AC-TEM) image of the CEI formed on the NCM811 positive electrode. Left: AC-TEM image; right: corresponding high-resolution TEM image of the CEI layer formed after 50 cycles at 25 °C in a Li||2.5 mAh cm^{-2} NCM811 cell (0.5C charge/1C discharge, 3-4.3 V) with SRCE electrolyte.

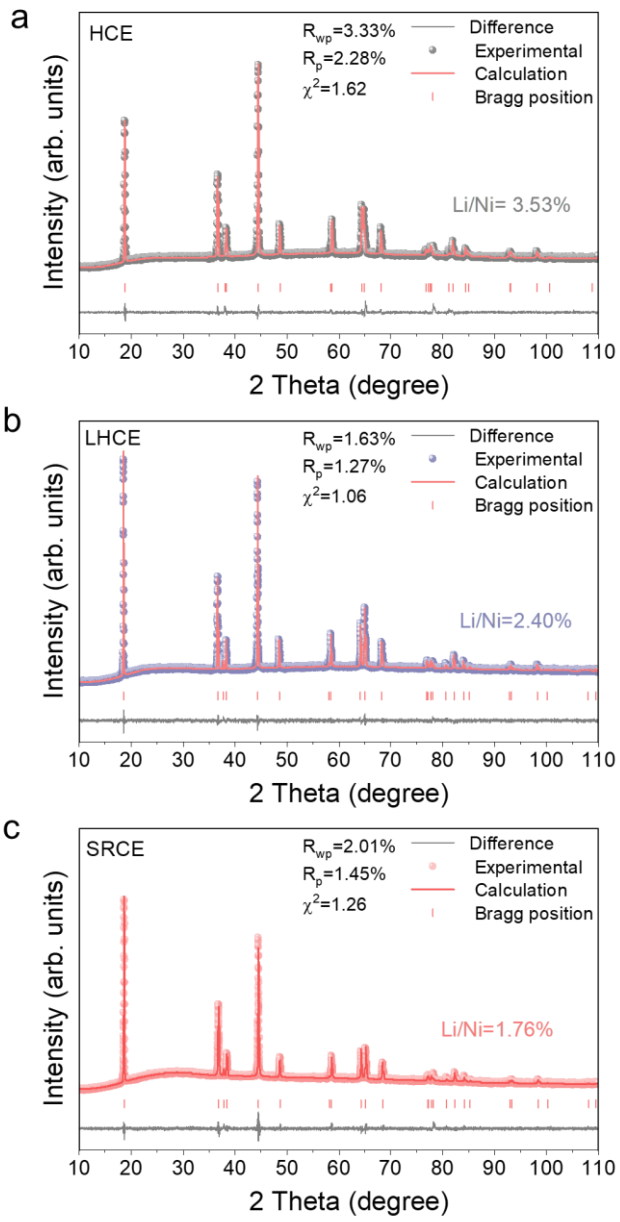

Supplementary Figure 24. Comparative analysis of the long-term structural stability of NCM811 positive electrodes. Rietveld-refined XRD patterns of the NCM811 positive electrodes extracted from Li||2.5 mAh cm^{-2} NCM811 half cells after 500 cycles (0.5C charge/1C discharge, 3-4.3 V) in (a) HCE, (b) LHCE, and (c) SRCE.

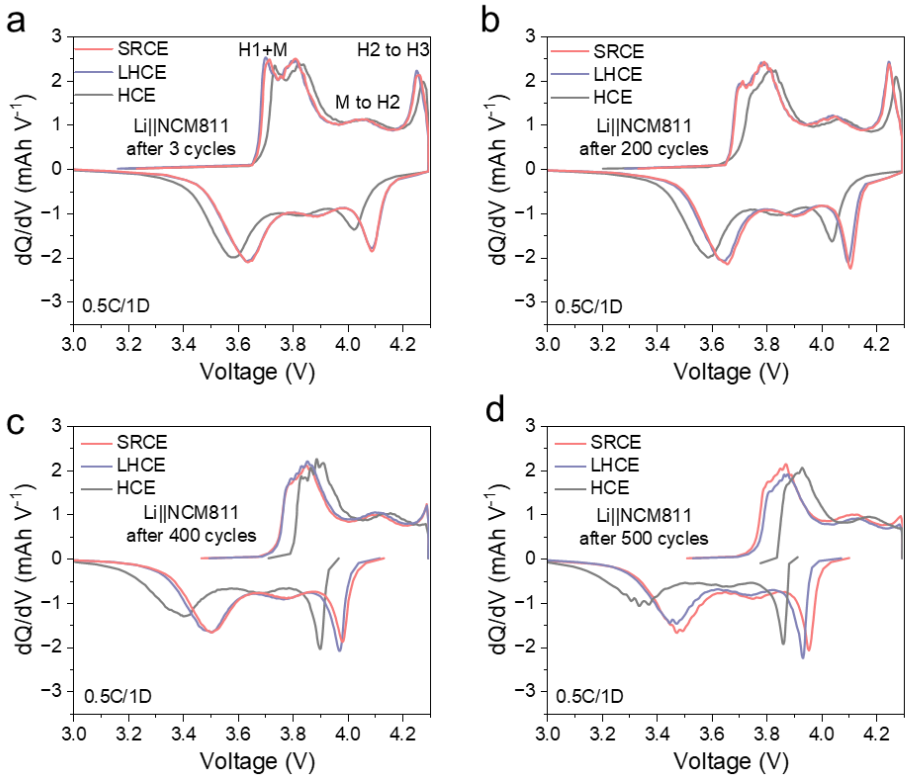

Supplementary Figure 25. Tracking NCM811 positive electrode degradation kinetics via dQ/dV analysis. Plots of the incremental capacity (dQ/dV) for Li||2.5 mAh cm^{-2} NCM811 half cells at 25°C (3-4.3 V, 0.5C charge/1C discharge) in three electrolytes at different cycle numbers of (a) 3^{rd}, (b) 200^{th}, (c) 400^{th}, and (d) 500^{th} cycle.

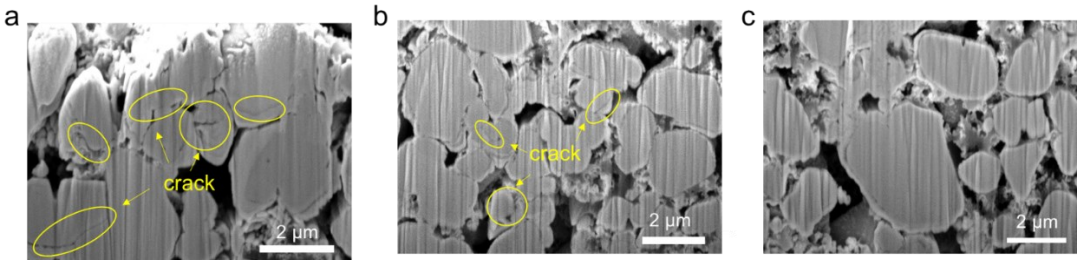

Supplementary Figure 26. FIB-SEM analysis of positive electrode structure. Cross-sectional SEM images of NCM811 positive electrode from Li||2.5 mAh cm^{-2} NCM811 half cells after 500 cycles (3-4.3 V, 0.5C charge/1C discharge) in (a) HCE, (b) LHCE, and (c) SRCE.

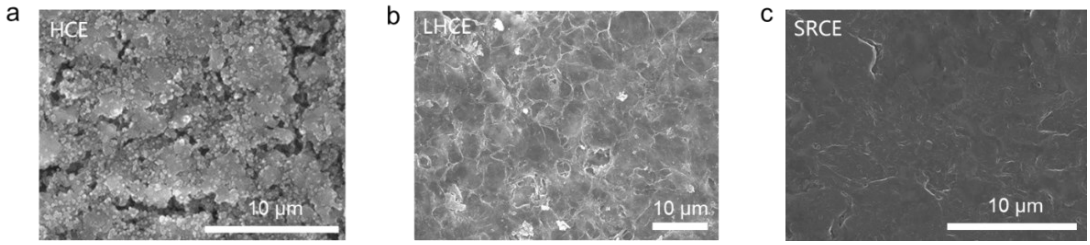

Supplementary Figure 27. Morphology of Li metal negative electrodes after cycling. SEM images of Li negative electrodes from Li||2.5 mAh cm^{-2} NCM811 cells after 100 cycles (3-4.3 V, 0.5C charge/1C discharge) in (a) HCE, (b) LHCE, and (c) SRCE.

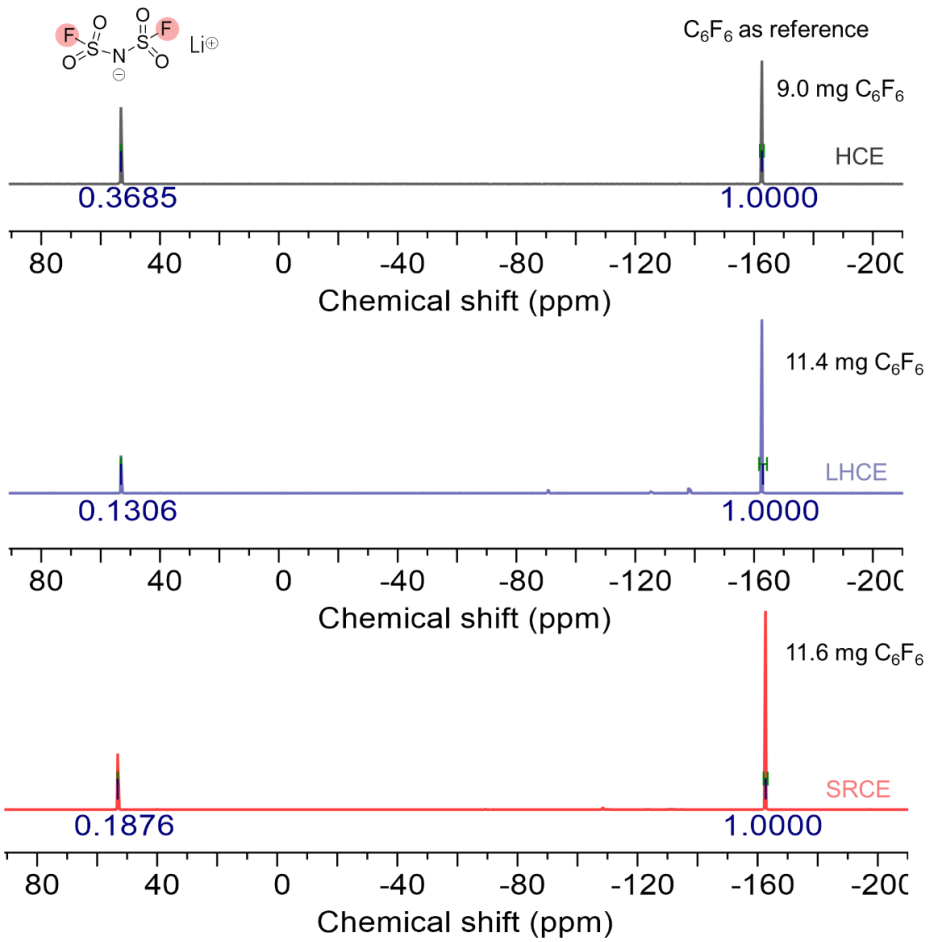

Supplementary Figure 28. The stacked ^{19}F quantitative NMR full spectrum of the HCE, LHCE, and SRCE after 200 cycles at 25℃ in 50μm Li||2.5 mAh cm^{-2} NCM811 cells (3-4.3 V, 0.5C charge/1C discharge), using C_6F_6 as the internal reference and DMSO-d_6 as solvent.

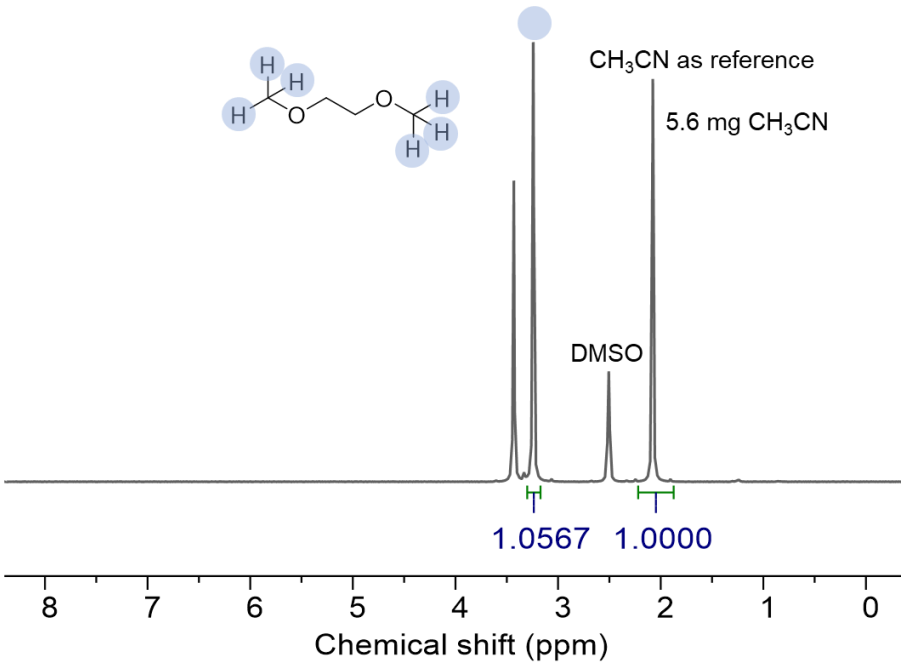

Supplementary Figure 29. Quantitative analysis of DME solvent consumption in HCE after cycling. The ^{1}H quantitative NMR spectrum of DME from the HCE electrolyte recovered from a 50μm Li||2.5 mAh cm^{-2} NCM811 cell after 200 cycles (3-4.3 V, 0.5C charge/1C discharge) at 25°C, using acetonitrile (CH_3CN) as an internal reference and dimethyl sulfoxide (DMSO-d_6) as the solvent.

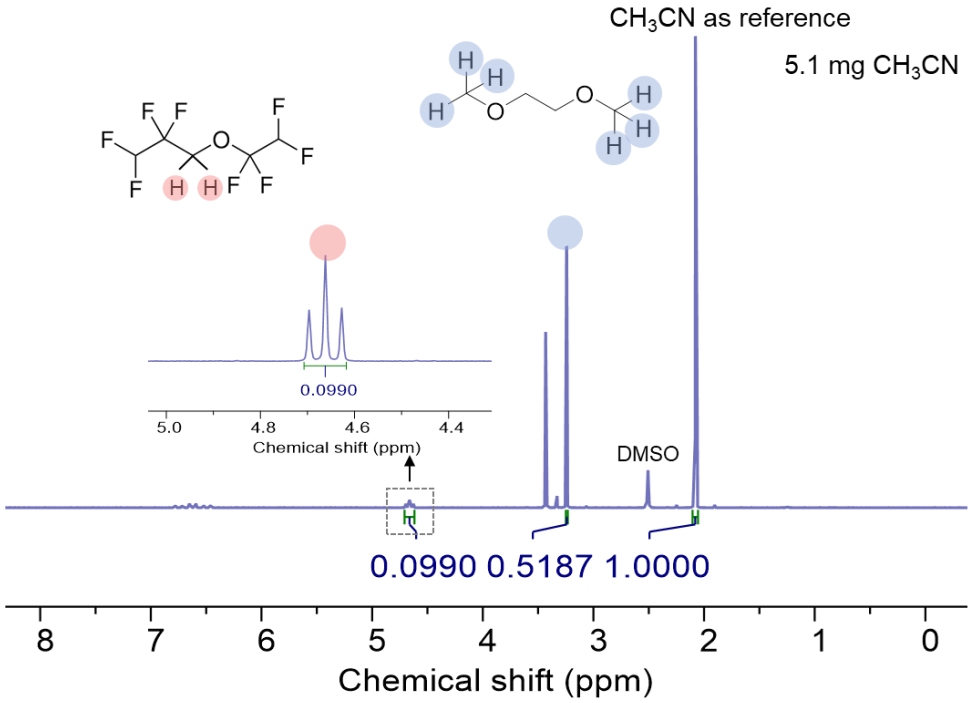

Supplementary Figure 30. Quantitative analysis of DME and TTE consumption in LHCE after cycling. The ^{1}H quantitative NMR spectrum of DME and TTE from the LHCE electrolyte recovered from a 50μm Li||2.5 mAh cm^{-2} NCM811 cells after 200 cycles (3-4.3 V, 0.5C charge/1C discharge) at 25℃, using acetonitrile (CH_3CN) as an internal reference and dimethyl sulfoxide (DMSO-d_6) as the solvent.

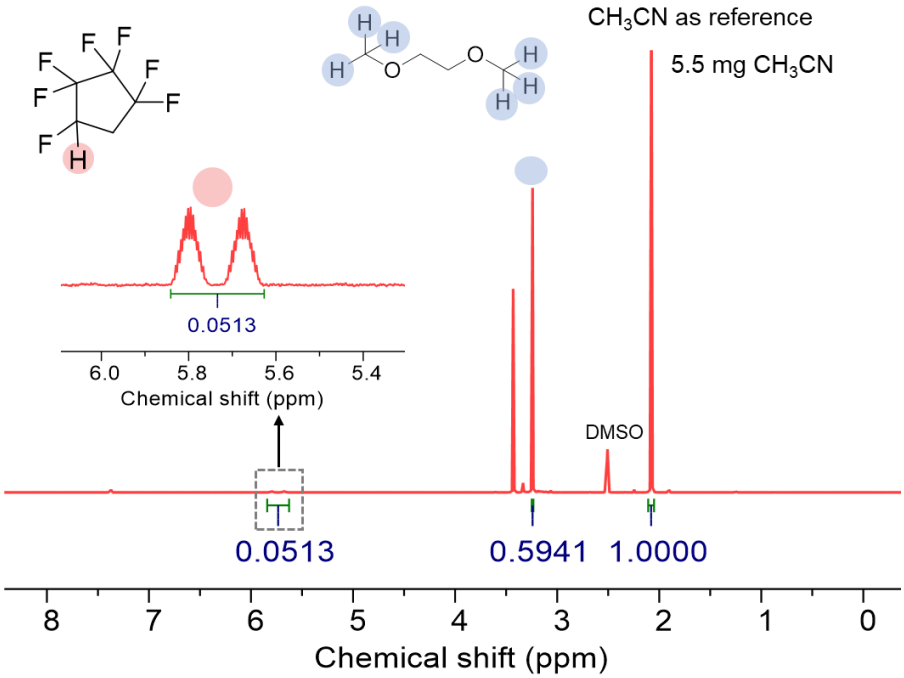

Supplementary Figure 31. Quantitative analysis of DME and HFC consumption in SRCE after cycling. The ^{1}H quantitative NMR spectrum of DME and HFC from the SRCE electrolyte recovered from a 50μm Li||2.5 mAh cm^{-2} NCM811 cells after 200 cycle (3-4.3 V, 0.5C charge/1C discharge) at 25℃, using acetonitrile (CH_3CN) as an internal reference and dimethyl sulfoxide (DMSO-d_6) as the solvent.

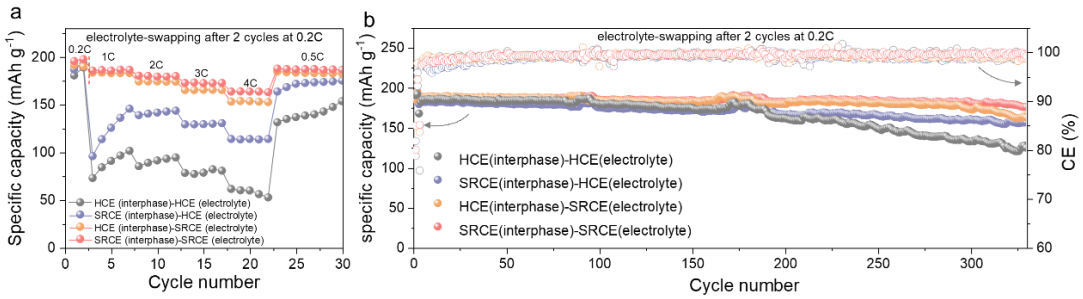

Supplementary Figure 32. Cross-swap experiments. (a) Rate performance of 50 μm Li||2 mAh cm^{-2} NCM811 coin cells at 25°C in cross-swap configurations, where X (interphase)-Y (electrolyte) denotes electrodes pre-cycled in electrolyte X and transferred into fresh electrolyte Y after two formation cycles. (b) Long-term cycling performance of 50 μm Li||2 mAh cm^{-2} NCM811 coin cells after cross-swapping at 25°C. Note: To exclude any artifacts arising from the cell disassembly procedure, all cells were subjected to an identical disassembly and reassembly protocol, including those for which the bulk electrolyte was kept unchanged before and after the swap. 1C= 200 mA g^{-1}.

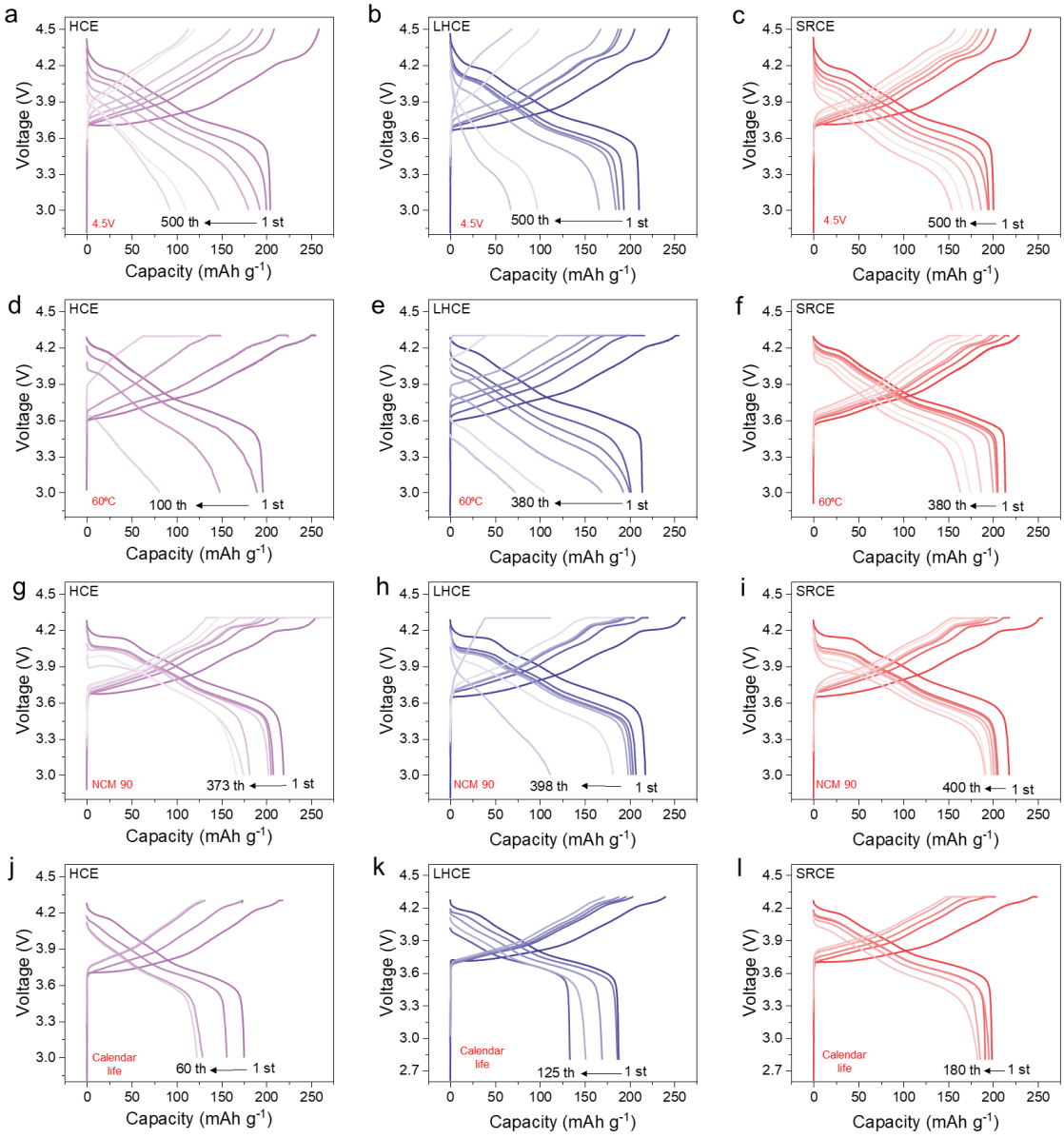

Supplementary Figure 33. Electrochemical performance of high-energy Li||NCM cells under various stringent conditions. (a-c) High voltage: 50 μm Li||2.5 mAh cm^{-2} NCM811 coin cells cycled between 3.0-4.5 V (0.5C charge/1C discharge) at 25°C. (d-f) Elevated temperature: 50 μm Li||2.5 mAh cm^{-2} NCM811 coin cells cycled between 3.0-4.3 V (0.5C charge/1C discharge) under 60°C operation. (g-i) High-nickel content: 50 μm Li||2 mAh cm^{-2} NCM90 coin cells cycled between 3.0-4.3 V (0.5C charge/1C discharge) at 25°C. (j-l) Calendar aging at 25°C: 50 μm Li||2.5 mAh cm^{-2} NCM811 coin cells operated under calendar aging (cycling with a 24 h resting interval after each charge).

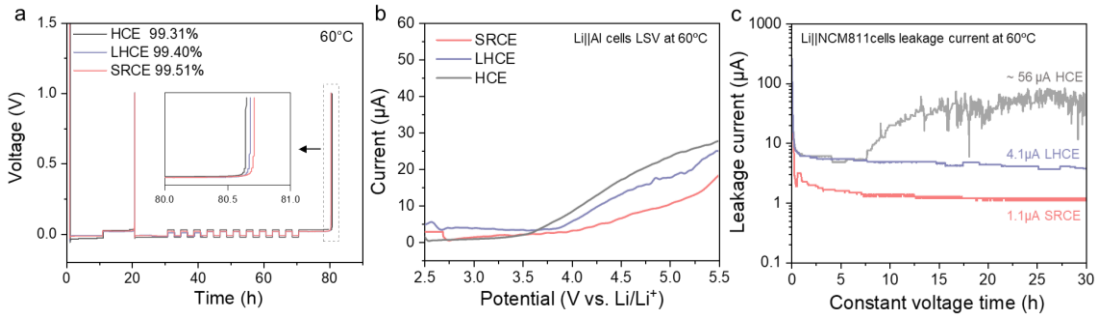

Supplementary Figure 34. Comparison of the stability of the negative electrode and positive electrode in different electrolytes at 60 °C. (a) Li plating/stripping CE at 60 °C, measured using the modified Aurbach method. (b) Linear sweep voltammetry (LSV) curves of Li||Al cells measured at 0.5 mV s^{-1} at 60 °C. (c) Leakage current profiles of Li||NCM811 cells at 60 °C, holding at 4.3 V for 30 h.

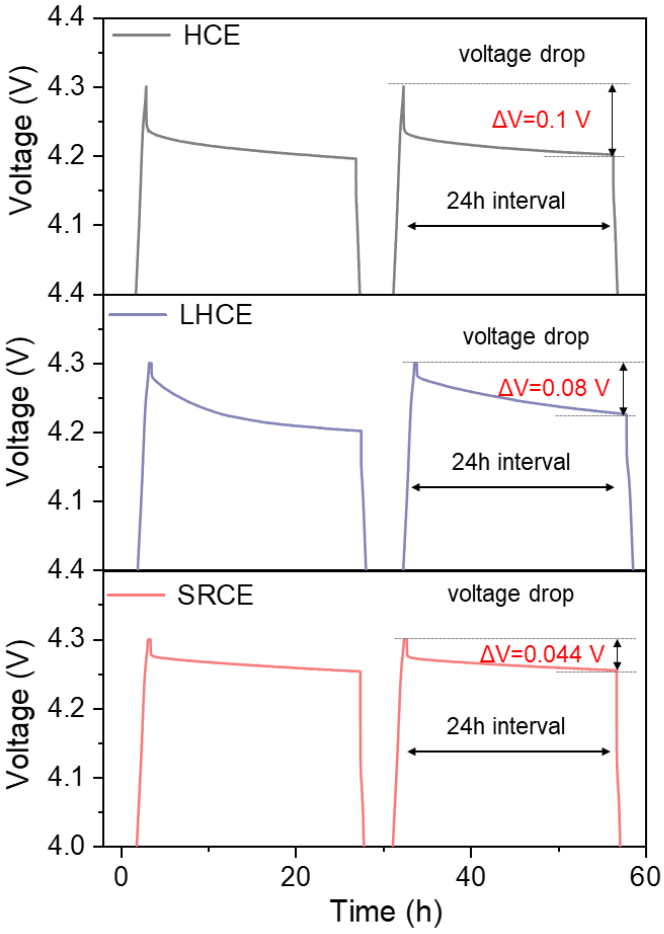

Supplementary Figure 35. Voltage decay during calendar aging. Voltage drops of 50 μm Li||2.5 mAh cm^{-2} NCM811 coin cells at 25°C during the resting period at high voltage (the 1st and 2nd cycles).

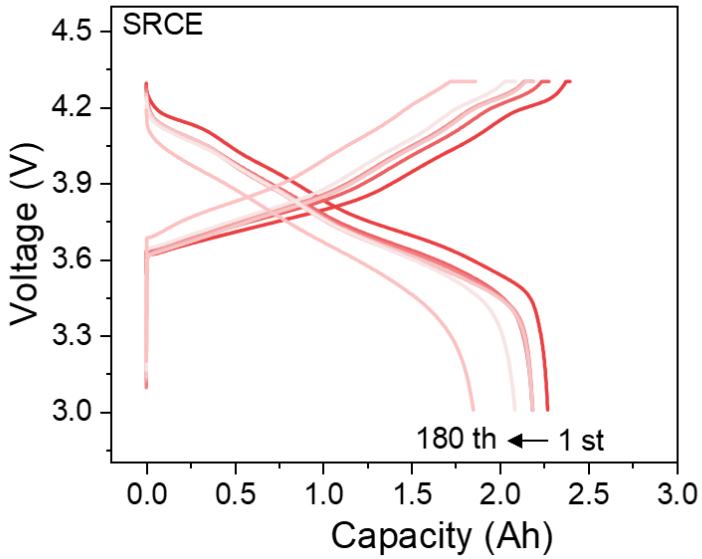

Supplementary Figure 36. Galvanostatic charge-discharge profiles of a 2.2 Ah pouch cell at 25°C at selected cycle numbers.

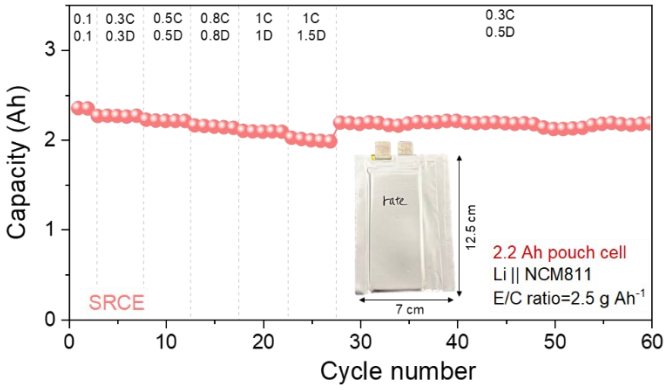

Supplementary Figure 37. Rate performance of a 2.2 Ah Li||NCM811 metal pouch cell at 25°C.

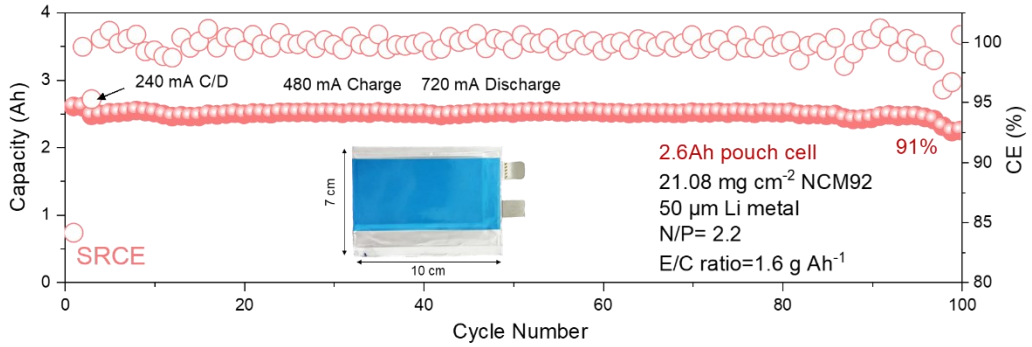

Supplementary Figure 38. Cycling performance of a 2.6 Ah Li metal pouch cell with SRCE at 25°C (3-4.3 V). The cell achieves a high specific energy of 475 Wh kg^{-1} (based on the total mass of the pouch cell) and retains 91% of its initial capacity after 100 cycles.

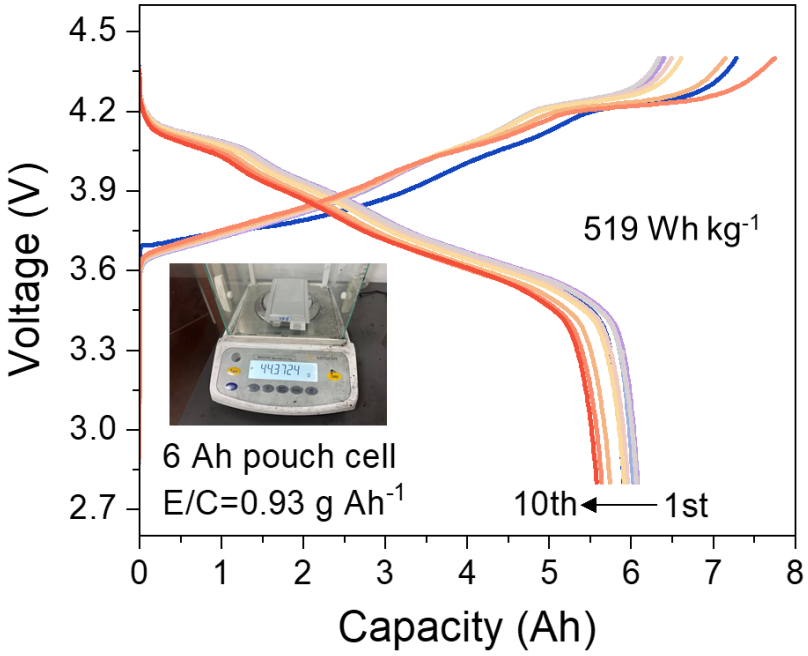

Supplementary Figure 39. Cycling performance of a 6 Ah-level Li||NCM95 metal pouch cell with SRCE. Galvanostatic charge–discharge voltage profiles of the cell at 25 °C in the voltage range of 3-4.3 V. Insert: photograph of the pouch cell showing its total mass. The specific energy is calculated based on the total mass of the entire pouch cell (Wh kg^{-1}).

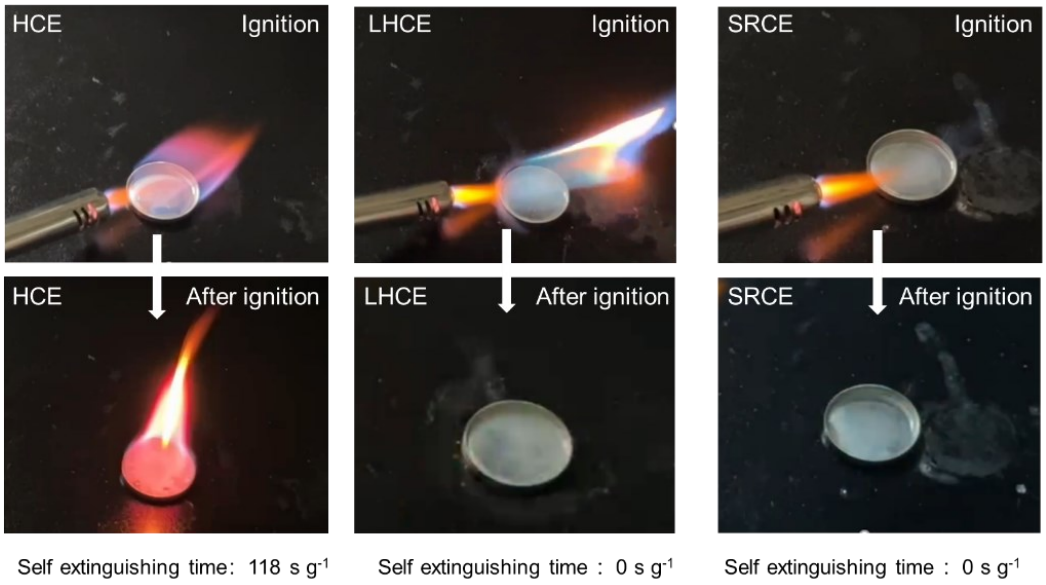

Supplementary Figure 40. Flammability test of different electrolytes. Optical images of during ignition and after ignition, alongside measured self-extinguishing times.

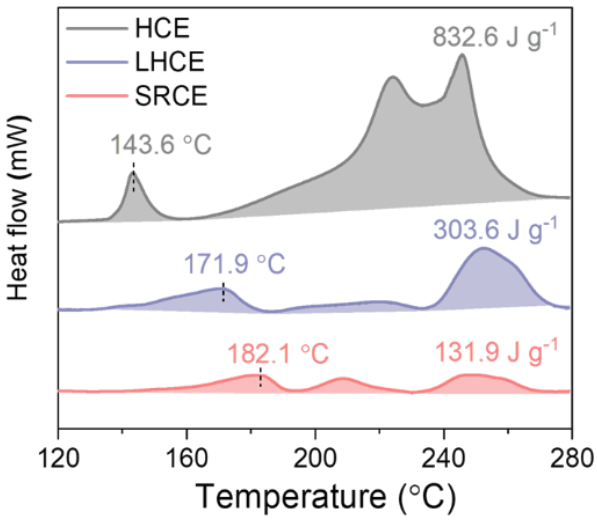

Supplementary Figure 41. Thermal stability of cycled NCM811 positive electrodes. Differential scanning calorimetry (DSC) traces of fully charged NCM811 positive electrodes retrieved from Li||2.5 mAh cm^{-2} NCM811 coin cells after 20 cycles at 25 °C (0.5C charge/1C discharge, 3-4.3 V) in HCE, LHCE, and SRCE. The electrodes were charged to 4.3 V at 0.1C before disassembly.

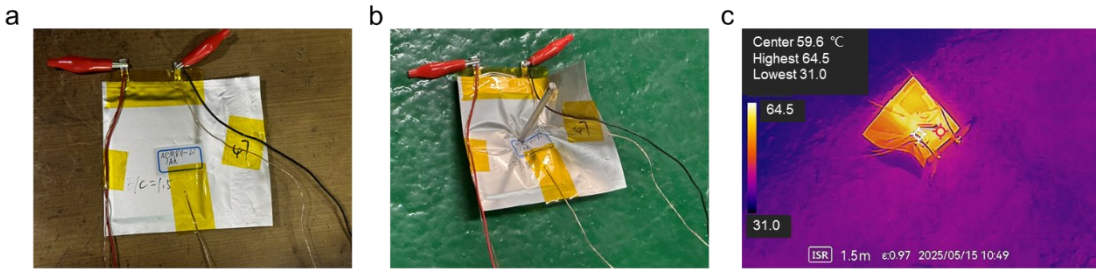

Supplementary Figure 42. Nail penetration safety test of a 1 Ah Li metal pouch cell with SRCE. (a, b) Optical photographs of the cell before and after the nail penetration test. (c) Infrared thermal image captured after the test. The maximum cell temperature remained below 60 °C during the test.

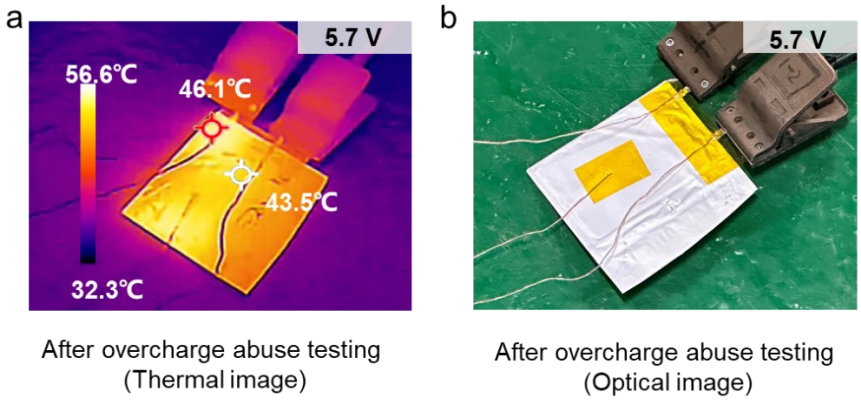

Supplementary Figure 43. Overcharge safety test of a Li metal pouch cell with SRCE. The cell was overcharged to 5.7 V and held for 2 hours. (a) Infrared thermal image and (b) optical photograph. No noticeable swelling, leakage, or thermal runaway was observed during the test.

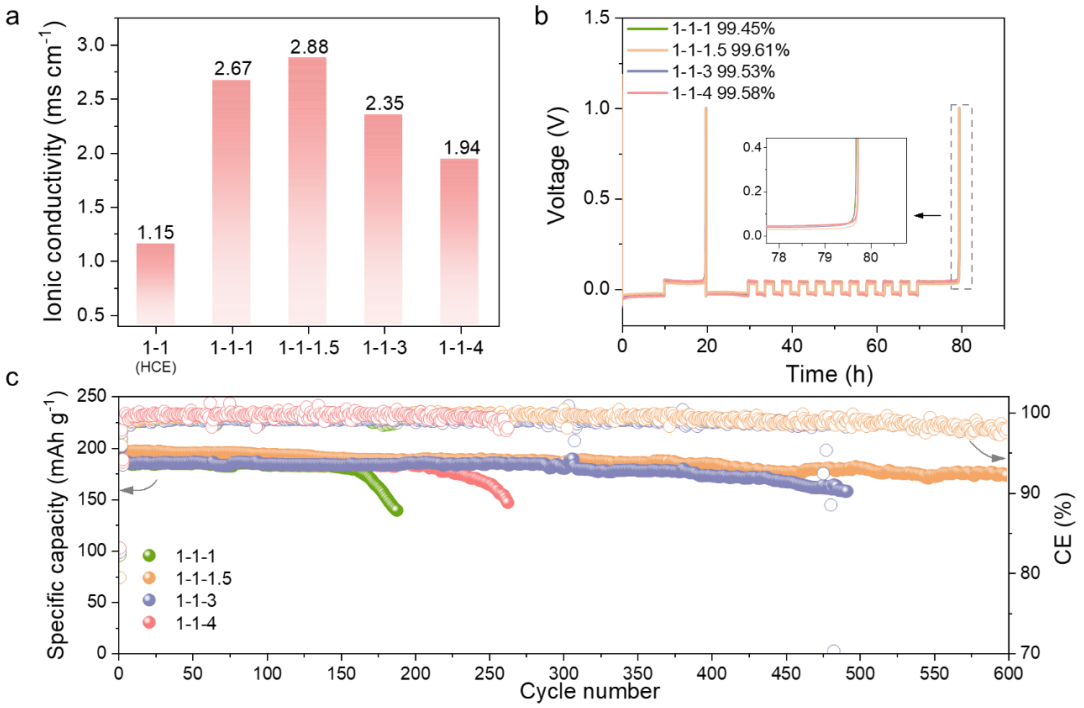

Supplementary Figure 44. **Screening for the optimal electrolyte ratio.** (a) Comparison of ionic conductivities for different electrolyte formulations at 25°C (*x-y-z* represents the molar ratio of LiFSI: DME: HFC). (b) Comparison of Li plating/stripping CE of Li||Cu cells at 25°C. (c) Long-term cycling stability of 50 μm Li||2.5 mAh cm^{-2} NCM811 coin cells at 25°C in different electrolytes.

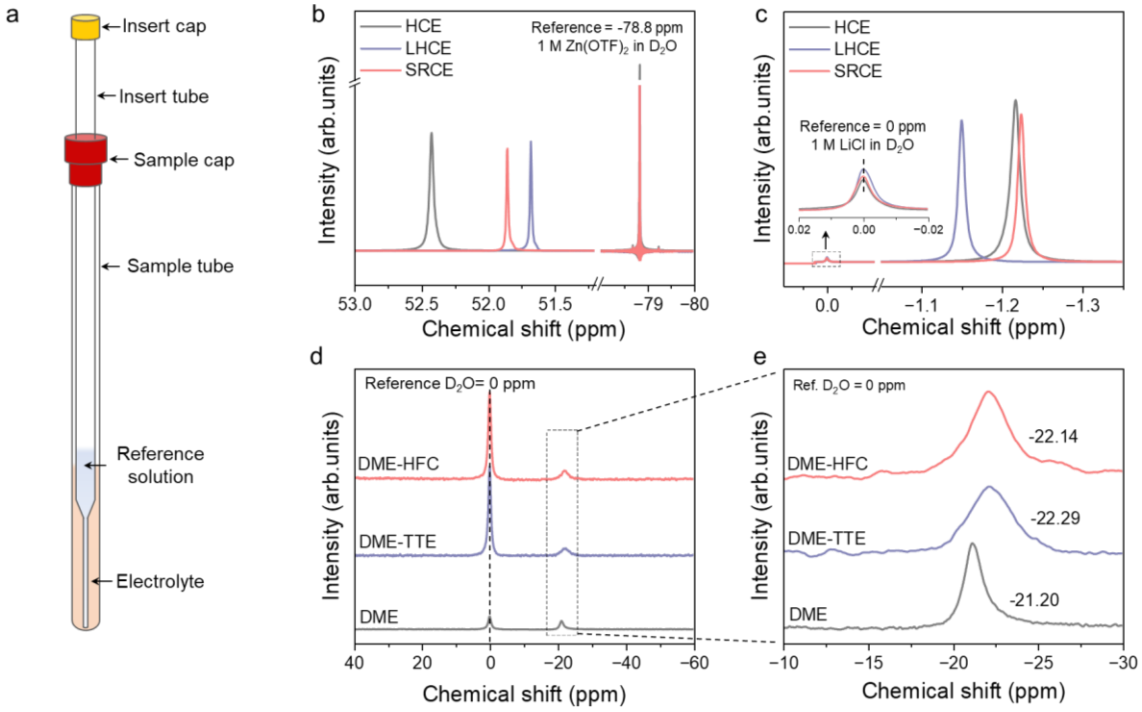

Supplementary Figure 45. Solvation structure characterization. (a) Schematic illustration of the coaxial NMR tube configuration. (b) ^{19}F NMR spectra of FSI^- in three electrolytes, with the external reference signal at -78.84 ppm for comparison (1 M $Zn(OTf)_2$ in D_2O). (c) ^{7}Li NMR spectra of the three electrolytes, referenced to 1 M LiCl in D_2O at 0 ppm. (d-e) ^{17}O NMR spectra of DME and its mixtures with TTE and HFC (external reference: D_2O at 0 ppm), with expanded views highlighting subtle chemical-shift differences.

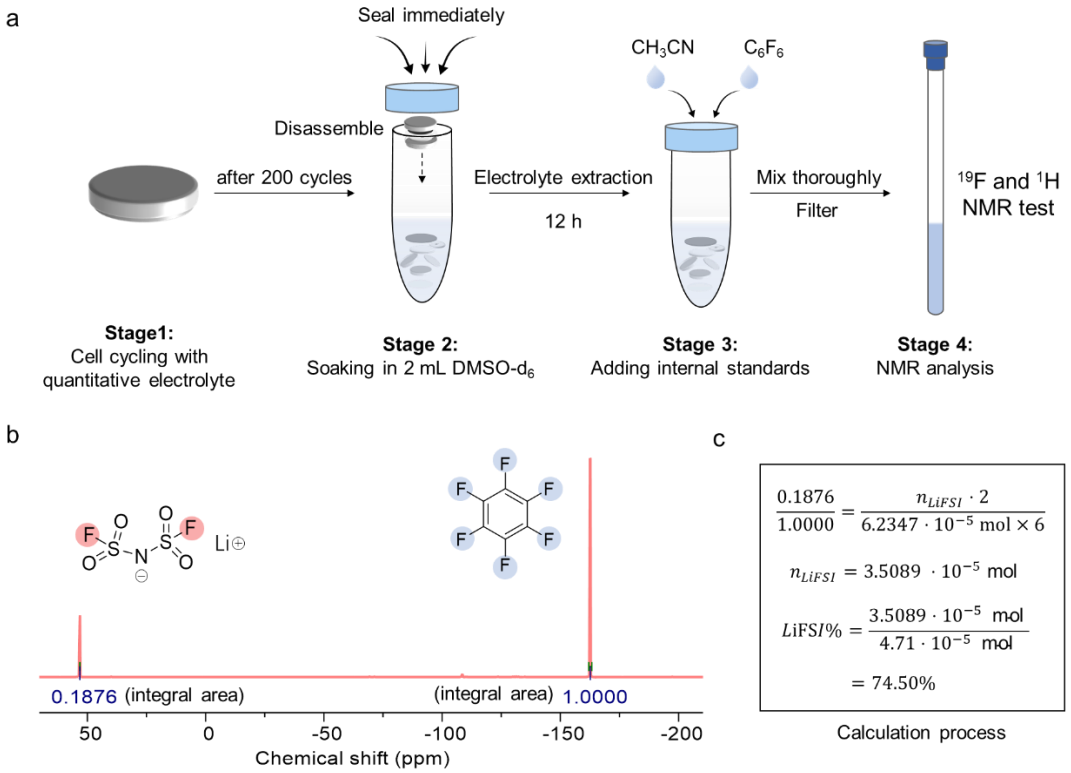

Supplementary Figure 46. Quantitative NMR analysis of the electrolyte consumption process. (a) Schematic diagram of the preparation process. (b) Quantitative ^{19}F NMR spectrum of the electrolyte achieved from the SRCE-based cell after 200 cycles, with peak integration performed using Mestre Nova software (hexafluorobenzene as internal standard). (c) Detailed calculation parameters and values for determining the residual amount of LiFSI in the SRCE electrolyte after cycling.

Supplementary Note 3.

Taking LiFSI consumption in SRCE as an example, the ^{19}F spectrum was processed with Mestre Nova software. As shown in **Supplementary Figure 46b**, the peak of hexafluorobenzene (δ = -162.6 ppm) was integrated and normalized to 1.0000 ($I_{C_6F_6}$), whereas the peak of LiFSI (δ = -53.19 ppm) was then integrated with a relative integral value of 0.1876 (I_{LiFSI}). Considering that one hexafluorobenzene molecule contains six equivalent fluorine atoms and one LiFSI molecule contains two equivalent fluorine atoms, the quantitative relationship is:

$$\frac{I_{LiFSI}}{I_{C_6F_6}} = \frac{2 \cdot n_{LiFSI}}{6 \cdot n_{C_6F_6}} \quad (1)$$

Thus, the remaining amount of LiFSI can be calculated as:

$$n_{LiFSI} = \frac{I_{LiFSI}}{I_{C_6F_6}} \times 3 \times n_{C_6F_6} \quad (2)$$

With the known mass of hexafluorobenzene added (11.6 mg, corresponding to 6.2347×10^{-5} mol), the remaining LiFSI was determined. The initial LiFSI content in the assembled cell was calculated based on the exact mass of electrolyte added (26.9 mg SRCE, containing 4.71×10^{-5} mol LiFSI). The LiFSI retention percentage was then obtained as (**Supplementary Figure 46c**):

$$Retention(\%) = (\frac{n_{LiFSI,remaining}}{n_{LiFSI,initial}}) \times 100\% \quad (3)$$

For ^{1}H NMR quantification of DME and HFC, acetonitrile (CH_3CN) was used as an internal standard following a similar calculation principle.

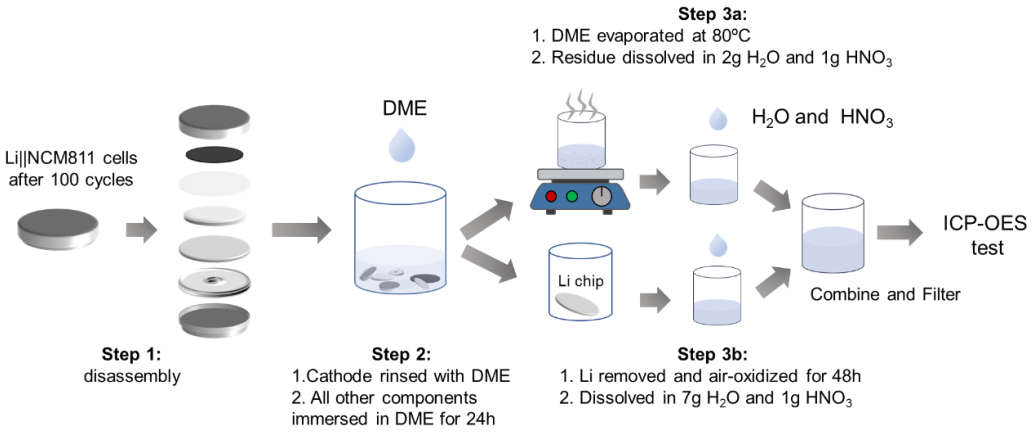

Supplementary Figure 47. Schematic diagram of the ICP-OES sample preparation process.

Supplementary Tables

Supplementary Table 1. The Hansen solubility parameter values of different solvents/diluents.

Solvent/Diluent	δD $(MPa)^{1/2}$	δP $(MPa)^{1/2}$	δH $(MPa)^{1/2}$	R_a to DME $(MPa)^{1/2}$	Miscible with HCE
DME	15.4	6.3	6.0	-	-
TTE	14.4	5.2	4.7	**2.63**	Yes
HFE	13.9	5.1	4.0	3.80	Yes
OTE	14.0	4.0	3.5	4.40	Yes
BTFE	13.7	4.4	3.0	4.92	Yes
HFC	14.3	2.8	2.1	5.68	Yes
PFP	12.8	3.7	1.5	**7.35**	No
1H-Perfluorohexane	12.8	2.1	1.6	8.00	No
Hexane	15.1	0.1	0.1	8.58	No
Perfluorohexane	12.1	1.0	0.4	**10.15**	No

Note: HFE (1,1,2,2-tetrafluoroethyl 2,2,2-trifluoroethyl ether); OTE (1H,1H,5H-octafluoropentyl-1,1,2,2-tetrafluoroethyl ether). PFP (Perfluoro(2-methyl-3-pentanone)).

Supplementary Table 2. Optical photographs of different diluents being miscible with HCE.

Diluent	**HFE**	**OTE**	**BTFE**	**HFC**
Miscible with HCE	 Miscible	 Miscible	 Miscible	 Miscible
Diluent	**PFP**	**1H-perfluorohexane**	**Hexane**	**Perfluorohexane**
Miscible with HCE	 **Immiscible**	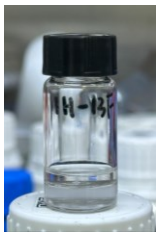 **Immiscible**	 **Immiscible**	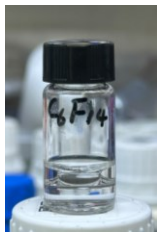 **Immiscible**

Supplementary Table 3. Physical properties of solvents and diluents. Key physicochemical parameters, including dielectric constant, density, boiling point, flash Point for the organic solvents and fluorinated diluents.

Properties	DME	TTE	HFC
Dielectric constant	7.3	6.2	1.97
Density (g cm^{-3})	0.863	1.434	1.492
Boiling Point (℃)	82-83	92	83
Flash Point (℃)	1	27.5	> 82.5

Supplementary Table 4. Coordination numbers (CNs) of Li^+ within the first solvation shell (r=3 Å) extracted from molecular dynamics (MD) simulations.

CNs	HCE	LHCE	SRCE
Li-O(DME)	2.15	1.70	1.77
Li-O(FSI^-)	2.81	3.57	3.51
Li-N(FSI^-)	0.10	0.09	0.10
Li-F(FSI^-)	0.06	0.03	0.06

Supplementary Table 5. Key transport properties of the electrolytes. Comparative data of the Li^+ self-diffusion coefficient, ionic conductivity, and Li^+ transference number for HCE, LHCE, and SRCE.

Electrolyte transport properties	HCE	LHCE	SRCE
Diffusion coefficient (10^{-11} m^2 s^{-1})	0.213	0.90	1.003
Ionic conductivity (mS cm^{-1})	1.15	2.42	2.88
Transference number of Li^+	0.35	0.38	0.55

Supplementary Table 6. Equivalent-circuit fitting parameters for the EIS spectra of Li‖NCM811 coin cells at the 20th and 400th cycles. (Supplementary Figure 16 d-e).

Electrolyte	Cycle number	Rsei (Ω)	Fitting error of R_{sei} (%)	Rct (Ω)	Fitting error of R_{ct} (%)
HCE	20	125.8	1.0359	42.8	1.4368
HCE	400	416.1	0.38915	93.4	1.3651
LHCE	20	69.9	0.80619	33.6	1.8183
LHCE	400	169.2	0.4209	32.2	1.9447
SRCE	20	66.3	0.80791	32.1	2.2259
SRCE	400	134.5	0.87554	41.3	1.9510

Supplementary Table 7. Atomic parameters from the Rietveld refinement of the Li||NCM811 half-cell after 500 cycles in HCE.

Atom	x	y	z	Occ.	Cell parameters
O1	0.0000	0.0000	0.2591	1.0000	
Li1	0.0000	0.0000	0.5119	0.4647	*a=2.8778 Å*
Mn1	0.0000	0.0000	0.0000	0.1000	*b=2.8778Å*
Co1	0.0000	0.0000	0.00000	0.1000	*c= 14.2172Å*
Ni1	0.0000	0.0000	0.0000	0.7647	*V=101.975 Å³*
Li2	0.0000	0.0000	0.0000	0.0353	*α=β= 90° γ=120°*
Ni2	0.0000	0.0000	0.5119	0.0353	

Supplementary Table 8. Atomic parameters from the Rietveld refinement of the Li||NCM811 half-cell after 500 cycles in LHCE.

Atom	x	y	z	Occ.	Cell parameters
O1	0.0000	0.0000	0.2592	1.0000	
Li1	0.0000	0.0000	0.50107	0.4760	*a= 2.8636 Å*
Mn1	0.0000	0.0000	0.0000	0.1000	*b= 2.8636Å*
Co1	0.0000	0.0000	0.0000	0.1000	*c= 14.2742Å*
Ni1	0.0000	0.0000	0.0000	0.7760	*V= 101.368 Å^3*
Li2	0.0000	0.0000	0.0000	0.0240	*α=β= 90° γ=120°*
Ni2	0.0000	0.0000	0.50107	0.0240	

Supplementary Table 9. Atomic parameters from the Rietveld refinement of the Li||NCM811 half-cell after 500 cycles in SRCE.

Atom	x	y	z	Occ.	Cell parameters
O1	0.0000	0.0000	0.25927	1.0000	
Li1	0.0000	0.0000	0.50107	0.4824	*a= 2.8633 Å*
Mn1	0.0000	0.0000	0.0000	0.1000	*b= 2.8633 Å*
Co1	0.0000	0.0000	0.0000	0.1000	*c= 14.28044 Å*
Ni1	0.0000	0.0000	0.0000	0.7824	*V= 101.393 Å^3*
Li2	0.0000	0.0000	0.0000	0.0176	*α=β= 90° γ=120°*
Ni2	0.0000	0.0000	0.50107	0.0176	

Supplementary Table 10. Specific parameters of the 2.2 Ah Li metal pouch cell.

Component	Parameter	Value
Positive electrode $LiNi_{0.8}Co_{0.1}Mn_{0.1}O_2$	Compaction density	3.45 g cm^{-3}
	Dimensions	46.9*106.4 mm^2
	Mass Loading (Single-sided)	22.4 mg cm^{-2}
	Collector	Al 12 μm
Negative electrode Li metal	Thickness	40 μm
	Compaction density	0.534 g cm^{-3}
Electrolyte	Weight	3.2 g
Separator	PE	2+12+2 μm
N/P ratio	-	1.82
Total mass	-	21.5 g
Discharge energy	at 0.1C	8.719 Wh
Specific energy (Based on the total mass of the pouch cell)	at 0.1C	405.2 Wh kg^{-1}

Supplementary Table 11. Specific parameters of the 2.6 Ah Li metal pouch cell.

Component	Parameter	Value
Cell	Number of layers	8
Positive electrode $LiNi_{0.92}Co_{0.03}Mn_{0.05}O_2$	Active material loading	95.6%
	Press density	3.3 g cm^{-3}
	Dimensions	44*85 mm^2
	Mass Loading (Single-sided)	21.09 mg cm^{-2}
	Collector	Al 10 μm
Negative electrode Li metal	Thickness (Single-sided)	50 μm
	Dimensions	47*88 mm^2
N/P ratio	-	2.4
Electrolyte	Weight	3.84 g
Separator	PE	2P + 12 + 3C + 2P
Total mass	-	21.0 g
Discharge energy	at 0.1C	9.979 Wh
Specific energy (Based on the total mass of the pouch cell)	at 0.1C	475.18 Wh kg^{-1}

Supplementary Table 12. Specific parameters of the 6 Ah-level Li metal pouch cell.

Component	Parameter	Value
Positive electrode $LiNi_{0.95}Co_{0.03}Mn_{0.02}O_2$	Active material loading	97 %
	Press density	3.2 g cm^{-3}
	Dimensions	54*122 mm^2
	Mass Loading (Single-sided)	25 mg cm^{-2}
	Collector	Al 12 μm
Negative electrode Li metal	Thickness	100 μm
	Dimensions	56*125 mm^2
N/P ratio	-	4.1
Electrolyte	Weight	5.6 g
Separator	Celgard	20 μm
Total mass	-	44.372 g
Charge energy	at 0.1C	25.454 Wh
Discharge energy	at 0.1C	23.060 Wh
Specific energy (Based on the total mass of the pouch cell)	at 0.1C	519 Wh kg^{-1}

Supplementary References

1. Ukhanev SA, Fedorov SV, Rusakov YY, Rusakova IL, Krivdin LB. Computational protocols for the ^{19}F NMR parameters. Part 2: Fluorobenzenes. *Journal of Fluorine Chemistry* **266**, 110093 (2023).
2. Cui Z*, et al.* Harnessing Rapid $Li^{+}/H\delta^{+}$ Exchange within the Electric Double Layer for High Performance Li-Ion Batteries. *Advanced Materials* **37**, e09735 (2025).
3. Shin W, Manthiram A. A Facile Potential Hold Method for Fostering an Inorganic Solid-Electrolyte Interphase for Anode-Free Lithium-Metal Batteries. *Angewandte Chemie International Edition* **61**, e202115909 (2022).